

• Original Paper •

Errors in Current Velocity in the Low-latitude North Pacific: Results from the Regional Ocean Modeling System

Xixi WEN^{1,2} and Wansuo DUAN^{*1,2}

¹*The State Key Laboratory of Numerical Modelling for Atmospheric Sciences and Geophysical Fluid Dynamics,
Institute of Atmospheric Physics, Chinese Academy of Sciences, Beijing 100029, China*

²*University of Chinese Academy of Sciences, Beijing 100049, China*

(Received 2 July 2018; revised 16 October 2018; accepted 29 October 2018)

ABSTRACT

Using the Regional Ocean Modeling System, this study investigates the simulation uncertainties in the current velocity in the low-latitude North Pacific where the Kuroshio originates [i.e., the beginning of the Kuroshio (BK)]. The results show that the simulation uncertainties largely reflect the contributions of wind stress forcing errors, especially zonal wind stress errors, rather than initial or boundary errors. Using the idea of a nonlinear forcing singular vector, two types of zonal wind stress errors (but sharing one EOF mode) are identified from error samples derived from reanalysis data as having the potential to yield large simulation uncertainties. The type-1 error possesses a pattern with positive anomalies covering the two zonal bands of 0°–15°N and 25°–40°N in the Pacific Ocean, with negative anomalies appearing between these two bands; while the type-2 error is almost opposite to the type-1 error. The simulation uncertainties induced by the type-1 and –2 errors consist of both large-scale circulation errors controlled by a mechanism similar to the Sverdrup relation and mesoscale eddy-like errors generated by baroclinic instability. The type-1 and –2 errors suggest two areas: one is located between the western boundary and the meridional 130°E along 15°–20°N, and the other is located between 140°–150°E and along 15°–20°N. The reduction of errors over these two areas can greatly improve the simulation accuracy of the current velocity at BK. These two areas represent sensitive areas for targeted observations associated with the simulation of the current velocity at BK.

Key words: Kuroshio, nonlinear forcing singular vector, targeted observation

Citation: Wen, X. X., and W. S. Duan, 2019: Errors in current velocity in the low-latitude North Pacific: Results from the Regional Ocean Modeling System. *Adv. Atmos. Sci.*, **36**(4), 397–416, <https://doi.org/10.1007/s00376-018-8140-4>.

Article Highlights:

- Identification of errors that significantly disturb the current velocity at the beginning of the Kuroshio (BK).
- Explanation of the mechanisms for the evolution of the errors.
- Determination of possible sensitive area for targeted observations for simulation at BK.

1. Introduction

The Northern Equatorial Current bifurcates into the southward-flowing Mindanao Current and the northward-flowing Kuroshio Current after encountering the Philippine coast. The Kuroshio Current flows northward along Luzon Island, Taiwan Island, and the southern coast of Japan before finally turning to the east at approximately 35°N and merging with the North Pacific Subtropical Gyre as the Kuroshio Extension. The Kuroshio Current is the western boundary current of the North Pacific Subtropical Gyre and transports seawater from the tropics to the subtropics (Latif and Barnett, 1994; Macdonald and Wunsch, 1996; Centurioni et al., 2004;

Zhai et al., 2014; Li et al., 2017). By exchanging heat and moisture with the atmosphere, the Kuroshio Current influences local and even global weather and climate; it may thus represent a precursory signal of weather and climate anomalies (Zhao and McBean, 1986; McCreary and Lu, 1994; Gu and Philander, 1997; Hu et al., 2015). In addition, when the Kuroshio Current passes by marginal seas such as the South China Sea and the East China Sea, it experiences momentum, heat and mass exchanges (Du et al., 2013; Nan et al., 2016; Li et al., 2017; Xiao et al., 2018). In particular, the Kuroshio Current intrudes into the South China Sea and takes different intrusion paths between Luzon Island and Taiwan Island (Nitani, 1972; Fang et al., 1998), which makes important contributions to the oceanic circulation, thermal field and ocean environment in the South China Sea (Qu et al., 2004; Nan et al., 2011; Du et al., 2013).

* Corresponding author: Wansuo DUAN
Email: duanws@lasg.iap.ac.cn

The region from east Luzon Island to east Taiwan Island was defined as the “beginning of the Kuroshio” (BK) by Nitani (1972). The current velocity at BK, especially the current velocity in the region where the Kuroshio Current originates, i.e., east of Luzon Island near 18°N , influences the different paths of Kuroshio Current intrusion into the South China Sea (Sheremet and Kuehl, 2007; Nan et al., 2011). Moreover, the annual mean value of the meridional heat transport in the Pacific peaks at approximately 18°N (Trenberth and Caron, 2001; Wunsch, 2005), and most of the poleward transport is contributed by the Kuroshio Current (Hu et al., 2015). As reviewed above, the velocity of the western boundary current east of Luzon Island at 18°N is important and is marked in Fig. 1. Therefore, it is of concern in the present study, and we refer to it as a representative of the current velocity at BK.

Considering the importance of the current velocity at BK, field observations have been conducted there. Previously, observations were only conducted using the discontinuous shipboard acoustic Doppler current profiler (Kashino et al., 2009) or indirect calculations using conductivity–temperature–depth data (Hu and Cui, 1991). Hu et al. (2013) deployed the acoustic Doppler current profile to conduct continuous observations of the velocity structure of the Kuroshio Current near BK from November 2010 to July 2011. Lien et al. (2014) observed the velocity of the Kuroshio Current near BK and focused on the influence of mesoscale eddies on Kuroshio Current transport from June 2012 to June 2013. More continuous observations were obtained by different platforms in the Origins of Kuroshio and Mindanao Currents project, which is part of a US–Taiwan collaborative field program referred to as the Origins of Kuroshio and Mindanao Currents/Observation of Kuroshio Transports and their Variability (Rudnick et al., 2011; Jan et al., 2015). The observations at BK indicate that the northward-flowing Kuroshio Current is in the upper 500 m; meanwhile, a southward current, named the Luzon Undercurrent (Hu and Cui, 1991; Hu et al., 2013; Lien et al., 2015), occurs beneath it. Furthermore, it has been shown that the variability of Kuroshio Current transport at BK occurs on intraseasonal to interannual time scales, with seasonal variability being dominant (Qiu and Lukas, 1996; Kim et al., 2004).

Current numerical models can simulate the essential fea-

tures of the Kuroshio Current at BK, including the velocity structure and variability of the Kuroshio Current transport. However, there are still notable differences between simulations and observations, particularly in terms of the current velocity (Lien et al., 2015). Hu et al. (2015) demonstrated that the poor simulation accuracy of the Kuroshio Current is ascribed to the low topographic resolution and the lack of observations associated with the Kuroshio Current. In addition, it is known that the available current observations are not sufficient for ocean models to simulate the ocean; therefore, reanalysis datasets, which do not exactly match the true state of the ocean, are often employed to derive the initial, boundary and forcing fields of a simulation. These fields, when derived from reanalysis data, obviously contain errors and will cause simulation uncertainties. Fujii et al. (2008) indicated that the initial error has an important effect on the prediction or simulation of the Kuroshio Current. Wang et al. (2013) and Zhang et al. (2016) also emphasized the prediction or simulation uncertainties in the Kuroshio Current induced by initial errors but from the perspective of initial error growth; specifically, they suggested that there are initial errors that have a particular structure and most perturb the prediction or simulation of the Kuroshio Current, which induce large prediction or simulation uncertainties. Zhang et al. (2017) demonstrated that by deploying “targeted observation” in the area where the most perturbing initial errors have large values, the prediction or simulation of the Kuroshio Current can be significantly improved [also see Zou et al. (2016)].

This so-called targeted observation method is a relatively new observational strategy that was developed in the 1990s. Its general idea is as follows: to better predict an event at a future time t_1 (verification time) in a focused area (verification area), additional observations are deployed at a future time t_2 (target time, $t_2 < t_1$) in some special areas (sensitive areas) where additional observations are expected to contribute to reducing the prediction errors in the verification area (Mu, 2013). These additional observations can be assimilated by a data assimilation system to form a more reliable initial state, which is then supplied to the model to obtain a more accurate prediction or simulation [see Fig. 1 in Majumdar (2016) for a schematic example for targeted observation].

Generally, targeted observation is used to decrease the

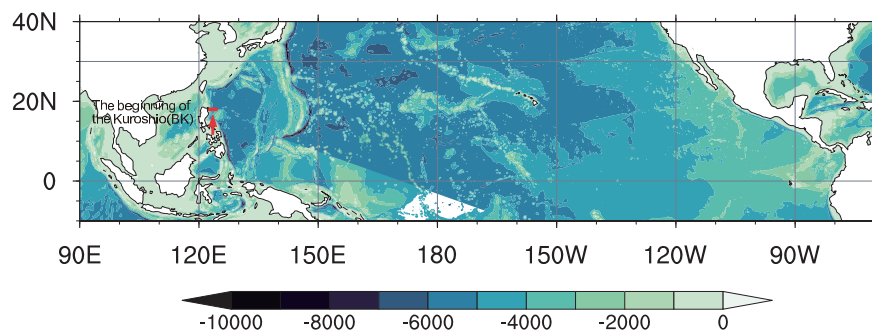


Fig. 1. Topography of the model domain (units: m). The red line pointed to by the red arrow is the section located at (18°N , 122° – 124°E), which represents the beginning of the Kuroshio (BK).

initial error and then greatly improve the prediction or simulation of the concerned events (Duan and Hu, 2016; Zou et al., 2016; Tao et al., 2017; Zhang et al., 2017). Nevertheless, when we simulate the current velocity at BK with a regional ocean model, reanalysis error appears in not only initial fields but also boundary and forcing fields. If the components of the boundary or forcing fields have a greater influence on the simulation than the components of the initial fields, it is necessary to extend the targeted observation to reduce the boundary and forcing errors. The key to targeted observation is to determine the sensitive area. According to previous studies (Duan and Hu, 2016; Zou et al., 2016; Tao et al., 2017; Zhang et al., 2017), the patterns of the most disturbing errors can provide clues to the identification of the sensitive area. These studies implied that the regions where the most disturbing errors show large values or where the prediction errors come from are potential sensitive areas. Thus, if we intend to extend the targeted observation to decrease the boundary and forcing errors, it is important to identify the most disturbing errors in boundary and forcing fields. Wang and Mu (2015) suggested that the most disturbing errors in boundary fields can be obtained by an extension of conditional nonlinear optimal perturbation. Duan and Zhou (2013) proposed the nonlinear forcing singular vector (NFSV) approach to obtain the most disturbing errors in forcing fields. Obviously, if boundary and/or forcing field errors are more important than initial errors for yielding simulation uncertainties, we can use the ideas of these two approaches to identify the most disturbing errors and then determine the sensitive area for targeted observation associated with boundary and/or forcing fields.

The above discussions naturally motivate us to consider the following questions: (1) Which one influences more significantly the simulation accuracy of the current velocity at BK among reanalysis errors in the initial fields, boundary fields or external forcing fields? (2) What are the most disturbing errors associated with the simulation uncertainties in the current velocity at BK? (3) What is responsible for the mechanism of the simulation uncertainties caused by these most disturbing errors? (4) What are the implications of these most disturbing errors for targeted observations associated with simulation of the current velocity at BK? The answers to these questions may help improve the simulation accuracy of the Kuroshio Current at BK.

The rest of this paper is organized as follows. The approach adopted to identify the most disturbing errors is described in section 2. The model configuration and data used in our study are presented in section 3. The performance of the model for the North Pacific and the BK is examined in section 4. Then, we investigate the simulation uncertainties in the current velocity at BK induced by initial, boundary and forcing errors in section 5 and the most disturbing errors in section 6. We further provide a possible mechanism responsible for the growth of the simulation error induced by the most disturbing error in section 7 and analyze the implications of the most disturbing errors in improving the simulation accuracy of the current velocity at BK in section 8. Finally, we present conclusions and a discussion in section 9.

2. NFSV approach

As mentioned in the introduction, the present study intends to explore the dominant error source of the simulation uncertainties in the current velocity at BK and identifies the most disturbing error to determine the sensitive areas for targeted observations associated with the simulation of current velocity at BK. In fact, among initial, boundary and forcing errors, zonal wind stress forcing errors are found to be the most important error source of the simulation uncertainties at BK (see section 5). Therefore, it is necessary to preferentially reduce errors in the zonal wind stress reanalysis data by identifying the most disturbing zonal wind stress forcing errors and exploring the corresponding targeted observations. To obtain the most disturbing wind stress forcing errors, it is reasonable to adopt the idea of the NFSV approach.

The NFSV approach is used to determine the forcing (or tendency) errors that lead to the largest prediction uncertainties in a nonlinear model (Duan and Zhou, 2013), which represent the most disturbing forcing errors. Using this approach, Duan and Zhao (2015) identified the most disturbing forcing error that causes significantly large prediction errors for El Niño events and demonstrated the applicability of the NFSV approach to reveal the most disturbing forcing errors. Next, we briefly describe the idea of the NFSV approach.

After denoting the state vector as \mathbf{B} , which represents the state variable of concern, we write the evolution equation of \mathbf{B} as follows:

$$\begin{cases} \frac{\partial \mathbf{B}}{\partial t} = F(\mathbf{B}(s, t)), \\ \mathbf{B}|_{t=0} = \mathbf{B}_0, \end{cases} \quad (1)$$

where $\mathbf{B}(s, t) = [\mathbf{B}_1(s, t), \mathbf{B}_2(s, t), \dots, \mathbf{B}_n(s, t)]$; \mathbf{B}_0 is the initial state; $(s, t) \in \mathcal{Q} \times [0, T]$, in which \mathcal{Q} is a domain in \mathbf{R}^n ; $\mathbf{s} = (s_1, s_2, \dots, s_n)$; t is time and $T < +\infty$; and F is a nonlinear operator. If the operator M_T is the propagator of Eq. (1), which “propagates” the state vector from an initial time to a future time T , we can write the solution to Eq. (1) as follows:

$$\mathbf{B}(s, T) = M_T(\mathbf{B}_0). \quad (2)$$

Equation (1) describes the evolution of a dynamic system without considering errors. In realistic predictions or simulations, both initial and model errors are inevitable. Denoting the state vector error as \mathbf{b} , its initial error as \mathbf{b}_0 and the model error as the constant tendency error vector $\boldsymbol{\varepsilon}(s)$, the forecast model of Eq. (1) is given as

$$\begin{cases} \frac{\partial(\mathbf{B} + \mathbf{b})}{\partial t} = F(\mathbf{B} + \mathbf{b}) + \boldsymbol{\varepsilon}(s) \\ \mathbf{B} + \mathbf{b}|_{t=0} = \mathbf{B}_0 + \mathbf{b}_0 \end{cases}. \quad (3)$$

We use $M_{T, \boldsymbol{\varepsilon}}$ to denote the propagator of Eq. (3). When $\boldsymbol{\varepsilon}(s) = 0$, $M_{T, \boldsymbol{\varepsilon}}$ is the same as M_T in Eq. (2). Thus, Eq. (3) can be written as

$$M_{T, \boldsymbol{\varepsilon}}(\mathbf{B}_0 + \mathbf{b}_0) = \mathbf{B}(s, T) + \mathbf{b}_{L, \boldsymbol{\varepsilon}}(s, T), \quad (4)$$

in which $\mathbf{B}(s, T) = M_{T, 0}(\mathbf{B}_0) = M_T(\mathbf{B}_0)$. It can easily be derived that $\mathbf{b}_{L, \boldsymbol{\varepsilon}}(s, T) = M_{T, \boldsymbol{\varepsilon}}(\mathbf{B}_0 + \mathbf{b}_0) - M_T(\mathbf{B}_0)$, which de-

scribes the prediction (or simulation) error caused by the initial and tendency errors. Without the influence of the initial error, the prediction (or simulation) errors are only caused by the tendency error and can be rewritten as $\mathbf{b}_{\boldsymbol{\varepsilon}}(\mathbf{s}, T) = M_{T, \boldsymbol{\varepsilon}}(\mathbf{B}_0) - M_T(\mathbf{B}_0)$.

Using these denotations, the NFSV $\boldsymbol{\varepsilon}_\mu$ can be obtained by

$$J(\boldsymbol{\varepsilon}_\mu) = \max_{\|\boldsymbol{\varepsilon}\|_a \leq \mu} J(\boldsymbol{\varepsilon}), \quad (5)$$

where the objective function J describes the prediction (or simulation) error and has the following form:

$$J(\boldsymbol{\varepsilon}) = \|M_{T, \boldsymbol{\varepsilon}}(\mathbf{B}_0) - M_T(\mathbf{B}_0)\|_c. \quad (6)$$

In Eqs. (5) and (6), $\|\cdot\|_a$ and $\|\cdot\|_c$ are two norms and the letters “ a ” and “ c ” indicates the norms are different. The prediction error J is measured by the norm $\|\cdot\|_c$, and the tendency error $\boldsymbol{\varepsilon}$ is measured by the norm $\|\cdot\|_a$, where the magnitude of $\boldsymbol{\varepsilon}$ is constrained by a positive number μ . Of course, this constraint can be given according to the physical problem of investigation.

3. Model configuration and data

The numerical model used in this study is the Regional Ocean Modeling System (ROMS), which was developed by Rutgers University and the University of California, Los Angeles. ROMS is a free-surface primitive equation ocean model with a terrain-following coordinate system and a horizontal generalized orthogonal curvilinear coordinate system (Haidvogel et al., 2000; Shchepetkin and McWilliams, 2003). This model includes various options to address model capabilities (Shchepetkin and McWilliams, 2005). These options include advection schemes with the options of second- and fourth-order centered differences and third-order, upstream-biased; a horizontal mixing process with the options of harmonic and biharmonic parameterizations; and vertical mixing with the options of Generic Length Scale mixing, Mellor–Yamada and K -profile parameterizations. Due to these flexible options, ROMS has been widely applied in oceanography studies to investigate basin-scale ocean circulation (Haidvogel et al., 2000, 2008), medium-scale ocean phenomena, such as the Kuroshio intrusion in the South China Sea (Lu and Liu, 2013), and the mesoscale oceanic response to tropical cyclones (Prakash and Pant, 2017).

In the present study, we explore the influence of reanalysis data errors on the simulation of the current velocity at BK. Therefore, the chosen model domain covers the tropical and subtropical Pacific and extends from 10°S to 40°N and 90°E to 290°E (Fig. 1). The horizontal resolution is 1/2° in both the zonal and meridional directions, and the vertical direction is divided into 20 sigma levels. The vertical coordinate system allows increased resolution near the surface by adjusting the values of the surface control parameter, theta_s, and the thickness of the surface layer, Tcline. The larger the value of theta_s, the more the resolution is kept above Tcline (Song and Haidvogel, 1994). Considering that the Kuroshio exists in the upper 500 m at BK (Hu et al., 2013; Lien et al., 2015),

we enhance the vertical resolution of the upper 500 m by setting the parameters as theta_s = 7.0 and Tcline = 500 m. The model topography is interpolated from the Earth topography five-minute grid (<https://www.ngdc.noaa.gov/mgg/global/etopo5.HTML>). The initial and boundary conditions are interpolated from NCEP’s Global Ocean Data Assimilation System (GODAS; Behringer and Xue, 2004), while the monthly forcing fields, including external wind stress forcing and heat flux, are interpolated from ERA-Interim (Dee et al., 2011). The fourth-order centered differences are selected to formulate the advection scheme. The biharmonic scheme is chosen to parameterize the horizontal mixing process, and the K -profile scheme is used to parameterize the vertical mixing process, where the horizontal diffusivity and viscosity coefficients are $6 \times 10^{10} \text{ m}^4 \text{ s}^{-1}$ and $8 \times 10^{11} \text{ m}^4 \text{ s}^{-1}$, respectively, and the vertical diffusivity and viscosity coefficients are $1.0 \times 10^{-5} \text{ m}^2 \text{ s}^{-1}$ and $1.0 \times 10^{-6} \text{ m}^2 \text{ s}^{-1}$, respectively.

For the data, in addition to the abovementioned reanalysis products of GODAS and ERA-Interim, some ocean reanalysis data and air–sea flux reanalysis data are also used in the present study. For the former, version 2.1.6 of the Simple Ocean Data Assimilation (SODA; Carton and Giese, 2008) and ECMWF’s Ocean Reanalysis System (ORA-S3; Balmaseda et al., 2008) are employed; for the latter, NCEP-R2 (Kanamitsu et al., 2002) and the Coordinated Ocean-ice Reference Experiments – Phase II (CORE.v2; Large and Yeager, 2009) are adopted.

4. Model validation

In the present study, we use ROMS with the configuration shown in section 3 to explore the simulation uncertainties of the current velocity at BK. Therefore, the performance of ROMS in simulating the BK and even the related North Pacific should be confirmed first. In addition, the current velocity at BK is strongly modulated by the westward propagating eddies. These eddies usually come from the Subtropical Countercurrent region, and baroclinic instability often excites the occurrence of these eddies (Lien et al., 2014; Zhang et al., 2017). Thus, the performance of ROMS for simulating baroclinic instability in the Subtropical Countercurrent region is also evaluated.

4.1. Validation for the North Pacific and BK

To investigate the performance of ROMS for the North Pacific and BK, we integrate the model with the initial condition generated from GODAS (January 1980), the boundary conditions from GODAS and the forcing conditions from ERA-Interim for the period 1980–2010. During the integration of ROMS, the total kinetic energy in the model domain reaches a stable state after one model year (i.e., the year 1980). Then, we evaluate the model integrations from the subsequent period of 1981 to 2010 to eliminate the initial adjustment process. The performance of ROMS is assessed against the monthly mean of the sea surface height (SSH) anomalies supplied by both the Archiving Validation and Interpolation of Satellite Oceanographic Data (AVISO;

www.avis0.altimetry.fr/) and GODAS. By applying EOF analysis to the monthly mean of the SSH anomalies derived from the integration of ROMS, AVISO and GODAS, we find that the first two EOF modes of the simulation of ROMS are consistent with those in AVISO and GODAS. Specifically, the first EOF mode exhibits a zonal dipolar pattern with poles located to the west and east of 180° (Figs. 2a, c and e) and has annual variability (Fig. 2g), while the second EOF mode presents a meridional tripolar pattern with poles located at approximately 10°S – 5°N , 5° – 20°N , and north of 20°N (Figs. 2b, d and f) and shows seasonal variability (Fig. 2h). These results indicate that ROMS can reasonably reproduce the SSH anomalies and that it has the ability to simulate large-scale motion in the model domain.

The simulation of the Kuroshio Current at BK is also assessed. Because there are no long-term continuous observations at BK, we have to employ the reanalysis data from GODAS, SODA and ORA-S3 to determine whether ROMS can adequately simulate Kuroshio Current transport and velocity at BK. The Kuroshio Current transport is calculated by the northern transport at BK. Figure 3a shows the variations of the Kuroshio Current transport calculated from GODAS, ROMS, SODA and ORA-S3. The seasonal variability is dominant in both ROMS and GODAS, while it is not as significant in SODA and ORA-S3. According to observations and simulations provided by previous studies, the seasonal variability is the most dominant variability for the BK transports [see Fig. 4 in Rudnick et al. (2011) for observations; and Fig. 12c in Qiu and Lukas (1996) and Kim et al. (2004) for simulations]. Thus, the simulations of both ROMS and GODAS are

consistent with those of previous works. However, the values of the transports in ROMS are somewhat different from those in GODAS. Specifically, the Kuroshio Current transports in ROMS vary between 10 Sv and 30 Sv, while those in GODAS vary between 10 Sv and 50 Sv. Observations have indicated that the annual mean Kuroshio Current transport at BK is approximately 15 Sv, with fluctuations of 10 Sv [Gordon et al. (2014) and Fig. 7c in Lien et al. (2014, 2015)]. Obviously, the Kuroshio Current transport modeled in ROMS is closer to the observed transport than that in GODAS. In Figs. 3b–e, we plot the climatological meridional velocities at BK in GODAS, ROMS, SODA and ORA-S3, respectively. It is shown that ROMS, SODA and ORA-S3 can simulate that the southward Luzon Undercurrent occurs beneath the northward Kuroshio Current, while GODAS fails to do that. Moreover, the Kuroshio Current in ROMS is located in the upper 500 m, which is the closest to the observation (Hu et al., 2013; Lien et al., 2015). Compared with GODAS, SODA and ORA-S3, ROMS captures more features of the current velocity at BK. Therefore, ROMS is acceptable for investigating the simulation uncertainties in the current velocity at BK induced by reanalysis errors.

4.2. Validation for the baroclinic instability at the Subtropical Countercurrent region

According to shipboard surveys conducted by the Japan Meteorological Agency (Kaneko et al., 1998; Nakano et al., 2005), the Subtropical Countercurrent region possesses a relatively weak eastward Subtropical Countercurrent within 18° – 25°N in the upper 200 m and a westward-flowing North-

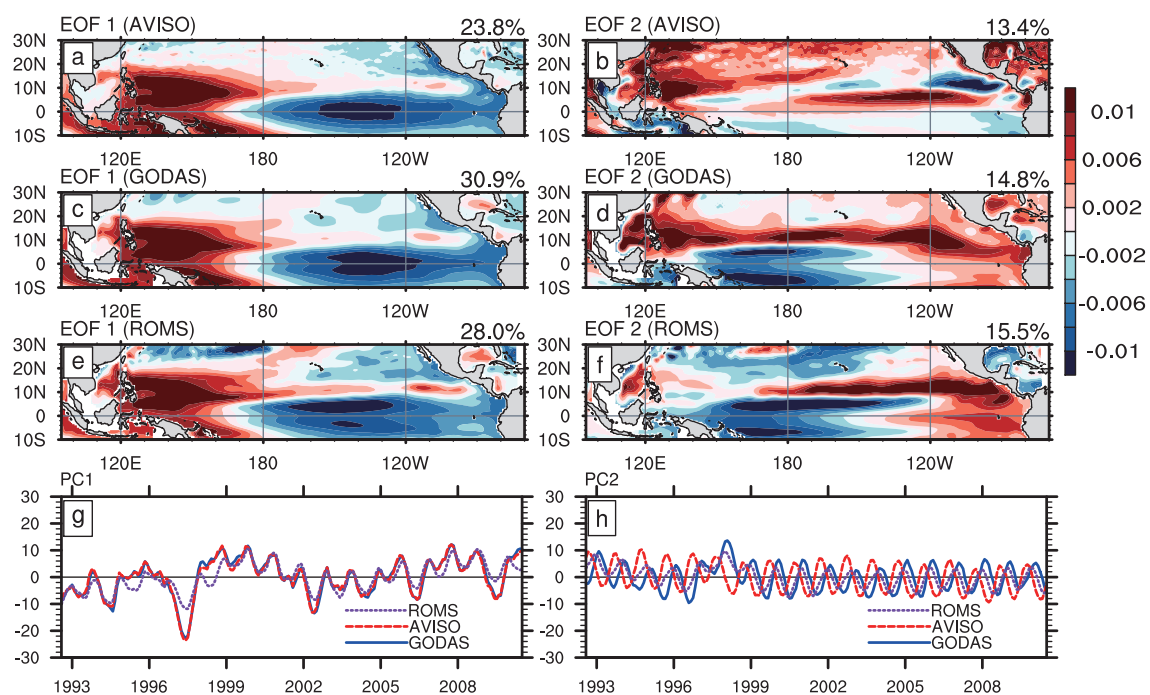


Fig. 2. The first two EOF modes of the Pacific SSH anomalies, which are derived from the data of (a, b) AVISO, (c, d) GODAS, and (e, f) the output of ROMS. Also shown are the corresponding time series of (g) EOF 1 and (h) EOF 2, where the time period is 1993–2010.

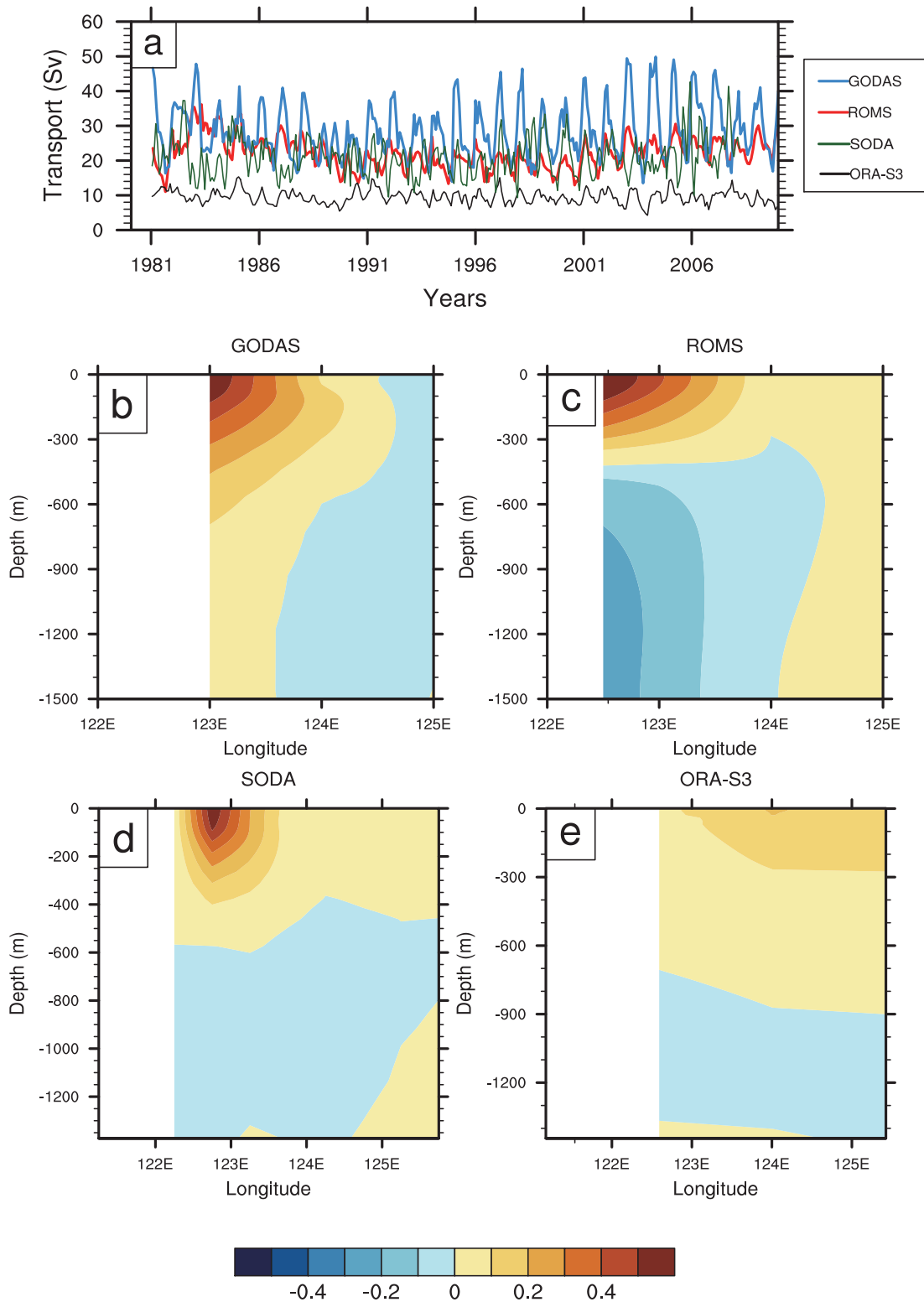


Fig. 3. (a) Time-dependent Kuroshio Current transport at BK calculated from GODAS (blue line), ROMS (red line), SODA (green line) and ORA-S3 (black line), and the climatological meridional velocity (units: m s^{-1} ; positive values indicate the velocity to be northward while the negative ones imply the velocity to be southward) at BK derived from (b) GODAS, (c) ROMS, (d) SODA, and (e) ORA-S3. The relevant time period is 1981–2010.

ern Equatorial Current beneath it [see Fig. 2a in Qiu et al. (2017)]. Therefore, the Subtropical Countercurrent region

exhibits the strong vertical shear of zonal velocity, which, together with the relatively weak stratification there, often

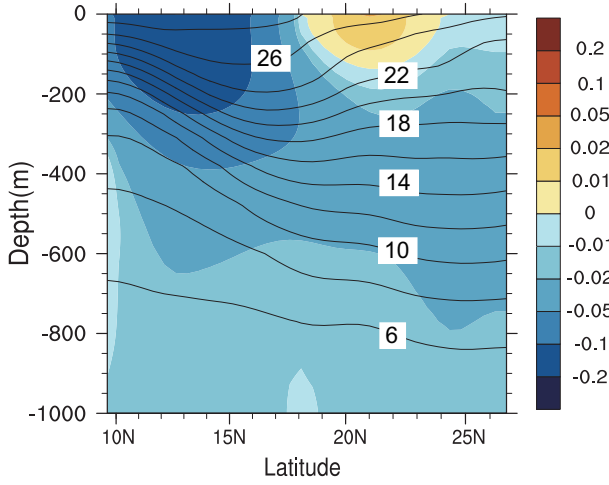


Fig. 4. Vertical structure of the climatological zonal velocity (shaded; units: m s^{-1}) and potential temperature (contours; units: $^{\circ}\text{C}$) along 140°E for 1981–2005.

induces baroclinic instability (Qiu, 1999; Qiu and Chen, 2010). This baroclinic instability often enhances westward propagating eddies that strongly modulate the current velocity at BK. To address the uncertainties of the current velocity at BK, it is necessary to examine whether ROMS can capture this mechanism.

The climatological vertical structure of the zonal velocity and potential temperature along 140°E in ROMS are plotted in Fig. 4. It is shown that the eastward Subtropical Countercurrent appears from the surface to the 22°C isotherm within 18° – 25°N and that beneath the Subtropical Countercurrent is the westward Northern Equatorial Current (and that the zonal velocity below the Northern Equatorial Current is relatively small). The isotherms within 18° – 25°N are sparser than those in the lower latitudes, which indicates relatively weak stratification in the Subtropical Countercurrent region. Therefore, the simulated zonal velocities in the 18° – 25°N section along 140°E in ROMS present a vertical structure of velocity shear and stratification similar to those observed along 137°E (Qiu and Chen, 2010; Qiu et al., 2017).

The 2.5-layer reduced-gravity model describes fluid motion with two active upper layers and a motionless third layer and can be used to approximately depict the fluid motion in the Subtropical Countercurrent region and the related baroclinic instability. Therefore, the 2.5-layer reduced-gravity model can be used to estimate the instability in the Subtropical Countercurrent simulated by ROMS. Using quasi-geostrophic approximation and linearization, the linear version of the potential vorticity equations associated with the 2.5-layer reduced-gravity model can be obtained as follows (Qiu, 1999; Qiu and Chen, 2010):

$$\frac{\partial q_{\kappa}}{\partial t} + U_{\kappa} \frac{\partial q_{\kappa}}{\partial x} + \frac{\partial \Pi_{\kappa}}{\partial y} \frac{\partial \phi_{\kappa}}{\partial x} = 0, \quad (7)$$

where q_{κ} is the potential vorticity perturbation, U_{κ} is the mean zonal flow of the control run, Π_{κ} is the mean potential vorticity of the control run, and ϕ_{κ} is the stream func-

tion perturbation in layer κ ($\kappa = 1$ and 2), t is the time, x and y are the coordinates of zonal and meridional directions. We assume that the eastward-flowing Subtropical Countercurrent is the first layer, which extends from the surface to the 22°C isotherm, and the westward-flowing Northern Equatorial Current is the second layer, which extends from the thermocline to the depth of no motion (i.e., the depth below which the absolute values of zonal velocities are less than 0.02 m s^{-1}); the layer below the depth of no motion is the stationary layer. For simplicity, U_{κ} is assumed to be constant and is obtained by taking the average eastward (westward) velocity in the first (second) layer. In addition, the variables in Eq. (7) can be expressed as

$$q_{\kappa} = \nabla^2 \phi_{\kappa} + \frac{(-1)^{\kappa}}{\lambda_{\kappa}^2} (\phi_2 - \phi_1 - \lambda_{\kappa} \phi_2), \quad (8)$$

$$\frac{\partial \Pi_{\kappa}}{\partial y} = \beta - \frac{(-1)^{\kappa}}{\lambda_{\kappa}^2} (U_1 - U_2 - \gamma_{\kappa} U_2), \quad (9)$$

where

$$\begin{cases} \gamma_{\kappa} \equiv \frac{\rho_{\kappa} - \rho_1}{\rho_3 - \rho_2} \\ \lambda_{\kappa}^2 \equiv \frac{(\rho_2 - \rho_1)}{\rho_0 f_0^2} g H_{\kappa} \end{cases}. \quad (10)$$

In Eqs. (8)–(10), H_{κ} is the mean thickness of the κ th layer; ρ_0 is the reference density of seawater, and ρ_{κ} is the mean density of the seawater in the κ th layer; f_0 is the Coriolis parameter; and β is the meridional gradient of the Coriolis parameter. The solution of Eq. (7) has the form of Eq. (11):

$$\phi_{\kappa} = \text{Re}(A_{\kappa} e^{(kx+ly-ct)i}), \quad (11)$$

where k and l are wavenumber in zonal and meridional directions, A_{κ} is amplitude of the stream function in the κ th layer and c is phase speed. Substituting Eq. (11) into Eq. (7) and using Eqs. (8)–(10), we can obtain the quadratic equation [Eq. (12)] for phase speed c , in which A_{κ} is nontrivial:

$$c^2 - \left(U_1 + U_2 - \frac{P+Q}{R} \right) c + \left(U_1 U_2 + \frac{\Pi_1 y \Pi_2 y}{R} - \frac{U_1 P}{R} - \frac{U_2 Q}{R} \right) = 0, \quad (12)$$

where

$$\begin{cases} P = \left(K^2 + \frac{1}{\gamma \delta \lambda^2} \right) \Pi_2 y \\ Q = \left(K^2 + \frac{1+\gamma}{\gamma \lambda^2} \right) \Pi_1 y \\ R = \left(K^2 + \frac{1+\gamma}{\gamma \lambda^2} \right) \left(K^2 + \frac{1}{\gamma \delta \lambda^2} \right) - \frac{1}{\gamma^2 \delta \lambda^4} \end{cases}, \quad (13)$$

the total wavenumber $K \equiv k^2 + l^2$ and $\delta \equiv H_1/H_2$. Since the evolving perturbations in the Subtropical Countercurrent region are distributed zonally, we set the meridional wavenumber $l = 0$ to satisfy them. Then, we can obtain the solution of Eq. (12) with the form $c = c_r + ic_i$. Equations. (11) and (12) indicate that the growth rate of the stream function perturbation denoted by Eq. (12) is kc_i . Therefore, the existence of the imaginary part c_i of solution c of Eq. (12) indicates that the concerned region exhibits instability, which, according to Qiu (1999), represents baroclinic instability.

Next, we use Eq. (7) to estimate the instability in the Subtropical Countercurrent region simulated by ROMS. To do this, Eq. (12) should be solved with the relevant parameters determined by the ROMS output. By using the output of the ROMS simulation shown in section 5, the parameters in Eq. (12) are computed by averaging the climatological mean over the Subtropical Countercurrent region (i.e., 17° – 20° N, 130° – 150° E) and are listed in Table 1. Using these predetermined parameter values, we obtain the values of the growth rate kc_i by Eq. (12) and plot them in Fig. 5 as a function of the wavenumber k and simulation times from January to December. The values of kc_i from January to December illustrate that they are positive, the maximum appears in March, and the minimum appears in August. These results indicate that baroclinic instability exists during the simulation period in the Subtropical Countercurrent region where eddy-like errors occur and that this instability is most significant in March, least significant in August, and presents seasonal variability. Such seasonal variability of the baroclinic instability agrees with the result in Qiu (1999), which indicates that ROMS has

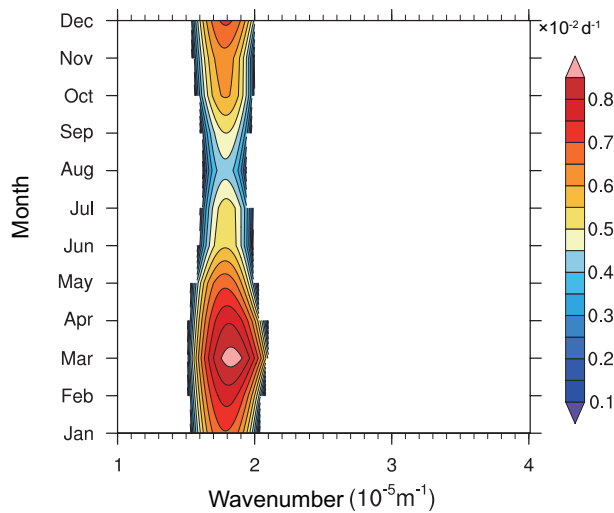


Fig. 5. Growth rate kc_i values for the perturbations in the region (17° – 20° N, 130° – 150° E) as a function of zonal wavenumber k calculated by Eqs. (11) and (12) using the parameters given in Table 1.

the capability to simulate the baroclinic instability in the region of the Subtropical Countercurrent in the observations.

In addition, Fig. 5 shows that kc_i depends on the wavenumber and only has positive values for wavenumber k values ranging from approximately $1.5 \times 10^{-5} \text{ m}^{-1}$ to $2.1 \times 10^{-5} \text{ m}^{-1}$. This result indicates that only a perturbation with a wavelength (which can be calculated by $2\pi/k$) ranging from 299 km to 419 km can be amplified due to baroclinic instability. Furthermore, we can obtain the wavelength of the fastest-growing perturbation by estimating the maximum positive kc_i value. Such wavelengths range from 355 km to 359 km (see Table 1). For convenience, we regard these wavelengths as the most unstable wavelengths.

5. Simulation uncertainties of the current velocity at BK caused by initial, boundary and forcing errors

As shown in section 4, with the given configuration ROMS can simulate the essential features of the current velocity at BK, large-scale SSH anomalies in the model domain and baroclinic instability in the Subtropical Countercurrent region. Therefore, we can assume that ROMS is perfect. Under the perfect model assumption, we explore the simulation uncertainties of the current velocity at BK induced by initial, boundary and forcing errors.

Starting on 1 January 1980, we integrate ROMS with the given configuration and obtain 25 one-year control runs for the period 1981–2005. These 25 control runs can be regarded as “true states”, and their perturbed simulations can be obtained by integrating ROMS with other configurations of initial or boundary conditions or forcing fields derived by superimposing errors on the given configuration. The other configurations, compared with the given configuration, can be thought of as perturbed ones of the given configuration, and obviously, the perturbations (or errors) superimposed on the given configuration are described by the differences between reanalysis datasets in the given configuration and other ones. Furthermore, these errors can be called “reanalysis errors” because the control runs with the given configuration are regarded as “true states”.

Table 1. Parameter values in Eq. (12) and the most unstable wavelength. The parameters are derived from the climatological mean for the period 1981–2005 and the most unstable wavelength is obtained from Eq. (12) (the units for U_k , H_k and ρ_k are m s^{-1} , m, and kg m^{-3} , respectively, while those for the most unstable wavelength is km).

Parameter	Jan	Feb	Mar	Apr	May	Jun	Jul	Aug	Sep	Oct	Nov	Dec
U_1	0.010	0.007	0.006	0.008	0.012	0.015	0.016	0.016	0.014	0.012	0.011	0.011
U_2	−0.037	−0.041	−0.043	−0.040	−0.035	−0.031	−0.028	−0.025	−0.024	−0.029	−0.032	−0.036
H_1	213.9	208.6	193.8	205.7	215.1	225.1	232.1	237.1	223.7	221.2	218.3	215.1
H_2	334.5	349.2	352.5	345.6	326.0	307.8	282.3	271.0	268.6	286.2	308.3	320.7
ρ_1	23.50σ	23.60σ	23.69σ	23.60σ	23.42σ	23.27σ	23.14σ	23.01σ	23.12σ	23.20σ	23.31σ	23.42σ
ρ_2	25.71σ	25.73σ	25.75σ	25.70σ	25.63σ	25.58σ	25.52σ	25.49σ	25.52σ	25.57σ	25.62σ	25.67σ
ρ_3	27.30σ	27.32σ	27.29σ	27.26σ	27.24σ	27.23σ	27.19σ	27.18σ	27.16σ	27.19σ	27.23σ	27.26σ
Most unstable wavelength	359	359	355	357	359	357	355	355	355	357	359	359

Since the simulations of the current velocity at BK are of concern in the present study, we focus on the roles of the errors of dynamically correlated SSH and zonal and meridional velocity in the initial and boundary conditions, as well as those of zonal and meridional wind stress in the forcing fields. The errors of these fields, as mentioned in the previous paragraph, are defined as the differences of the relevant fields between reanalysis datasets in the given configuration and other ones. We superimpose each of these (analysis) errors on the control runs and integrate ROMS to obtain the perturbed simulations. By comparing these perturbed simulations with the control runs, we can identify which errors yield much larger simulation uncertainties of the current velocity at BK. Specifically, the initial errors are obtained by subtracting the relevant fields in GODAS for every January in 1981–2005 from those in SODA and ORA-S3; the boundary condition errors are derived by subtracting the related fields in GODAS for 1981–2005 from those in SODA and ORA-S3; and the wind forcing errors are generated by subtracting the wind stress in ERA-Interim for 1981–2005 from those in NCEP-R2 and CORE.v2. All the data mentioned above are interpolated based on the grid configuration of the control runs before conducting the subtraction. For each variable, we can obtain two groups of error samples for initial and boundary conditions and forcing fields. Then, a total of 50 perturbed simulations (two groups of error samples \times 25 true states) can be obtained. The simulation errors of the current velocity at BK are measured by

$$\text{Error}(t) = \sum_{d,i,j} [v_{s,(d,i,j)}(t) - v_{c,(d,i,j)}(t)]^2, \quad (14)$$

where $v_{c,(d,i,j)}$ and $v_{s,(d,i,j)}$ represents the meridional velocity in the control run (represented by subscript c) and the perturbed simulation of control run (represented by subscript s) at grid point (d, i, j) , which is characterized by coordinates of depth, longitude and latitude; t represents time. The simulation errors of the current velocity at BK are calculated at the section located at $(18^\circ\text{N}, 122^\circ\text{--}124^\circ\text{E})$, which covers the range of the Kuroshio Current at BK in both the observations (Qu et al., 1998; Wang and Hu, 2012; Wang et al., 2015) and the ROMS simulation (Fig. 3c).

To illustrate the error that leads to the largest simulation uncertainties in the current velocity at BK, we perturb the components of the initial, boundary and forcing fields by using the given error samples (see previous paragraph) and estimate the simulation uncertainties caused by them, where the simulation uncertainties are estimated by Eq. (14).

The evolution of simulation uncertainties and the box-and-whisker plot of the simulation uncertainties are presented in Fig. 6. It is shown that the simulation uncertainties caused by the errors in concerned components do not have significant differences from each other before May. However, after May, the simulation uncertainties caused by the wind stress errors, especially the zonal wind stress errors, grow rapidly and tend to be obviously greater than those caused by initial and boundary errors (see Fig. 6a). In addition, the box-and-whisker plots in Figs. 6b and c indicate that most of the con-

trol runs show much larger simulation errors not only in December (i.e., the final time of the simulation period) but also in the annual mean when they are disturbed by zonal wind stress errors. In conclusion, zonal wind stress errors tend to cause much larger simulation uncertainties for most of the control runs and therefore need to be preferentially corrected to greatly improve the simulation accuracy of the current velocity at BK.

6. The zonal wind stress errors significantly disturb the current velocity at BK

Since the zonal wind stress errors tend to cause more considerable simulation uncertainties in the current velocity at BK, reducing the zonal wind stress errors may provide an efficient way to improve the simulation accuracy of the current velocity at BK. It has been suggested that conducting targeted observations in some specific regions and assimilating them to the model can reduce the errors in the zonal stress forcing field and greatly improve a simulation with limited observations (see the introduction). The key to targeted observation is to determine the areas where the additional observations are preferentially employed, i.e., the sensitive areas for targeting, which are often identified by the region where the most disturbing error has large values. As such, to effectively reduce the zonal wind stress errors by assimilating the targeted observations, we should first find the most disturbing zonal wind stress error and, according to the region where the large errors concentrate, determine the sensitive areas for the simulation of the current velocity at BK. In actuality, the NFSV approach has been suggested to calculate the most disturbing forcing errors (see section 2). Nevertheless, since the present study focuses on the effect of reanalysis errors (as derived from available reanalysis datasets) on the simulation of current velocity at BK, the NFSV (i.e., the most disturbing forcing errors) here should be identified from the analysis error samples (see section 5; for convenience, we denote the set consisting of these error samples as “ \mathbf{E} ”). That is, the constraint condition of the tendency errors $\boldsymbol{\varepsilon}$ in Eq. (5) should make the tendency errors belong to the set \mathbf{E} . Section 5 has shown that the zonal wind stress forcing errors, compared with initial and boundary errors, cause much larger simulation uncertainties for most of the control runs. Then, we can use Eq. (5) and particularly establish the optimization problem for computing the most disturbing zonal wind stress error:

$$J_{\boldsymbol{\varepsilon}\mu} = \max_{\boldsymbol{\varepsilon} \in \mathbf{E}} \|M_{T,\boldsymbol{\varepsilon}}(\mathbf{B}_0) - M_T(\mathbf{B}_0)\|_c, \quad (15)$$

where the constraint condition is particularly prescribed as $\boldsymbol{\varepsilon} \in \mathbf{E}$, and the other denotations are the same as in Eq. (5).

To solve the NFSV, the gradient of the related objective function with respect to the tendency error plays an important role in the solution procedure and is obtained with the help of the adjoint method (Duan and Zhou, 2013). The adjoint module requires large amounts of computing resources and time. However, the present study only considers the reanalysis errors derived from the available reanalysis datasets.

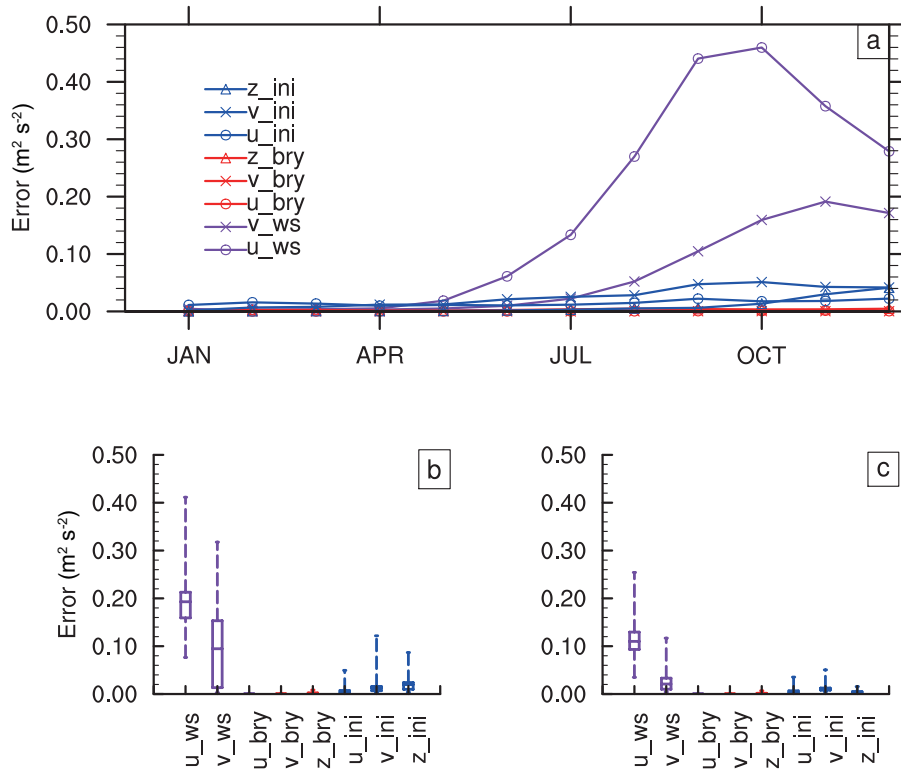


Fig. 6. (a) Evolution of the simulation uncertainties in the current velocity at BK caused by initial errors (blue lines), boundary errors (red lines) and external wind stress forcing errors (purple lines). The simulation uncertainties are averaged for the 25 control runs. Box-and-whisker plot of (b) the simulation uncertainties in December and (c) the annual means of the simulation uncertainties with respect to the 50 perturbed simulations (2×25 control runs) caused by initial errors (blue boxes), boundary errors (red boxes) and wind stress forcing errors (purple boxes). The parameters z_ini , v_ini , and u_ini represent the SSH, meridional velocity, and zonal velocity components of the initial errors, respectively; z_bry , v_bry , and u_bry represent the SSH, meridional velocity and zonal velocity components of the boundary errors, respectively; and v_ws and u_ws represent the meridional and zonal components of the wind stress forcing errors, respectively.

Therefore, we can introduce an ensemble-based approach to compute the NFSV more efficiently. Specifically, by comparing the simulation errors caused by the forcing error samples in \mathbf{E} , we select the forcing error that causes the largest simulation error as an approximation of the NFSV. Of course, we must acknowledge that the error samples in the ensemble-based method are hardly ergodic and that the resultant NFSV depends on error samples and may not be the exact NFSV in Eq. (5) mathematically. Nevertheless, this result is the NFSV in Eq. (15). Therefore, for the sake of convenience, we denote the NFSV of zonal wind stress errors as “NFSV-like errors”.

To determine the NFSV-like errors, it is reasonable to take the differences between different reanalysis products as error samples for calculating the NFSV-like errors. In the present study, we take error samples from the differences between pairs of available ERA-Interim, NCEP-R2 and CORE.v2 monthly values during the period 1981–2005, which comprise 900 error samples (3×25 years \times 12 months). To extract the dominant structures of the 900 error samples, we apply EOF analysis to them and obtain the first 18 EOF patterns (which can explain over 90% of the variance of the total sam-

ples). We denote these EOF patterns and their negative phases as $\mathbf{p}'_{i,j}(m)$, with $m = 1, 2, 3, \dots, 36$, where i and j are coordinates corresponding to longitude and latitude, respectively. For $m = 1, 2, 3, \dots, 18$, the EOF patterns of the error samples correspond to EOF 1, EOF 2, EOF 3, \dots , EOF 18, while for $m = 19, 20, \dots, 36$, they correspond to the patterns of the negative phases of EOF 1, EOF 2, EOF 3, \dots , EOF 18. We scale $\mathbf{p}'_{i,j}(m)$ by $(\mathbf{p}'_{i,j})_{scale}(m) = \alpha \mathbf{p}'_{i,j}(m) / \|\mathbf{p}'_{i,j}(m)\|$, where the norm $\|\mathbf{p}'_{i,j}(m)\| = \sqrt{\sum_{i,j} \mathbf{p}'_{i,j}(m)^2}$, and $\alpha = 7.49 \text{ N}^2 \text{ m}^{-4}$ is the scale factor, which is the mean magnitude of the 900 zonal wind stress error samples. The magnitude of the zonal wind stress error is calculated by the norm of the error sample. The error samples $(\mathbf{p}'_{i,j})_{scale}(m)$ belong to set \mathbf{E} in Eq. (15). The 36 members of \mathbf{E} describe the main structures of the 900 error samples and are sufficiently diverse to estimate the uncertainties in the zonal wind stress errors.

The 25 control runs obtained in section 5 are employed as true states to be simulated. The members of \mathbf{E} are superimposed on each of the 25 control runs to obtain 900 perturbed simulations (36 members \times 25 control runs). Based on

these 900 perturbed simulations, we attempt to determine the NFSV-like zonal wind stress errors by estimating the simulation errors caused by the 36 error samples. We plot the evolution of the simulation errors and the box-and-whisker plot of the simulation errors in Fig. 7. This figure shows that the zonal wind stress errors of the pattern of EOF 13 and its opposite pattern tend to cause much larger simulation errors than those of other EOF patterns (see Fig. 7a). Furthermore, Figs. 7b and c show that such zonal wind stress errors, compared with those of the other EOF patterns, tend to cause most of the 25 control runs to have larger simulation errors. Thus, the zonal wind stress errors of the EOF 13 pattern and its opposite pattern have a more significant effect on the simulation uncertainties of the current velocity at BK and represent the NFSV-like zonal wind stress errors of the current velocity at BK.

The NFSV-like zonal wind stress errors of EOF 13 and its opposite pattern share one EOF mode but different growth behaviors (see section 7). To distinguish their differences and facilitate this description, we particularly denote the NFSV-like errors with the patterns of EOF 13 and its negative phase as type-1 and -2 errors, respectively. A type-1 error possesses a zonal wind stress error pattern with positive anomalies covering two bands (0° – 15° N and 25° – 40° N) across the Pacific basin and negative anomalies occurring in the region between the two bands, i.e., the band of 15° – 25° N across the Pacific basin (see Fig. 8, upper panel). A type-2 error exhibits a pattern similar to those of type-1 errors but with opposite signs (see Fig. 8, lower panel). However, why do the type-1 and -2 errors induce large simulation uncertainties in the current velocity at BK? What mechanism is responsible for their evolution? We will address these questions in the next section.

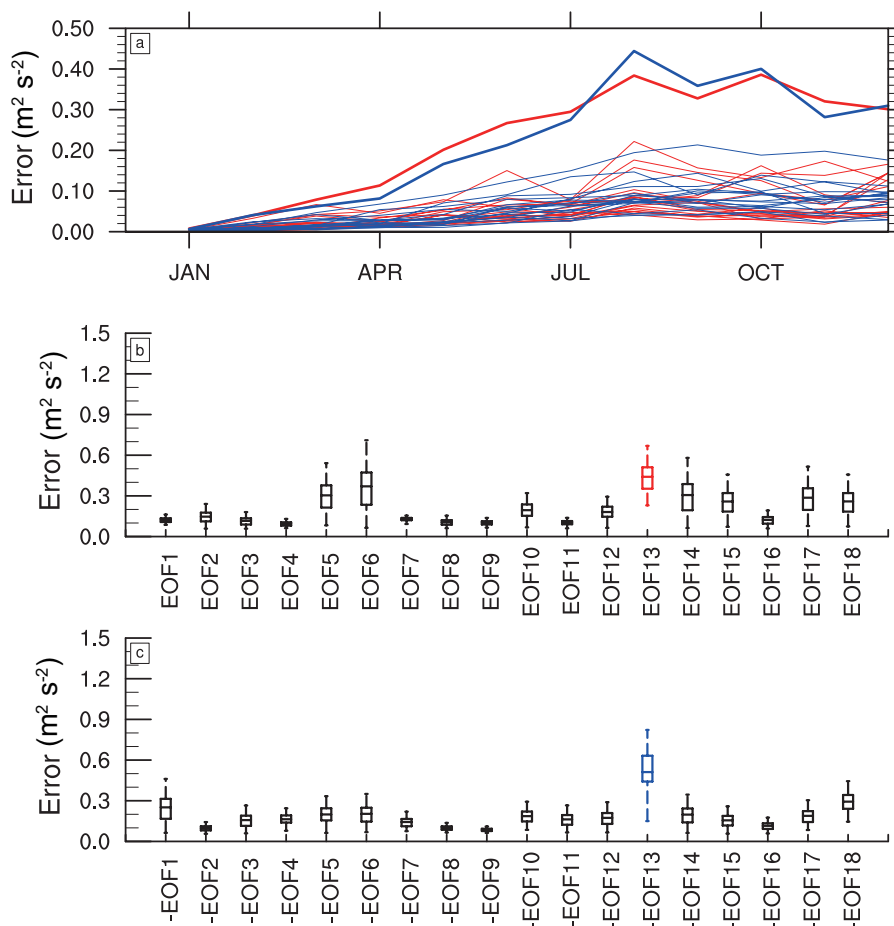


Fig. 7. (a) Evolution of the simulation errors in the current velocity at BK caused by the rescaled error samples in **E** with the EOF patterns (red lines) and their negative patterns (blue lines); the two bold lines represent the simulation errors caused by the error samples with the pattern of EOF 13 (red bold line) and its negative pattern (blue bold line), where the simulation errors are averaged for the 25 control runs. (b) Box-whisker plot of the simulation errors in December caused by the error samples of the EOF patterns with respect to the 25 control runs, where the red box represents that of the simulation error caused by the error sample with the pattern of EOF 13. (c) As in (b), but for the error samples with negative EOF patterns; furthermore, the blue box represents the simulation error caused by the error sample with the negative pattern of EOF 13.

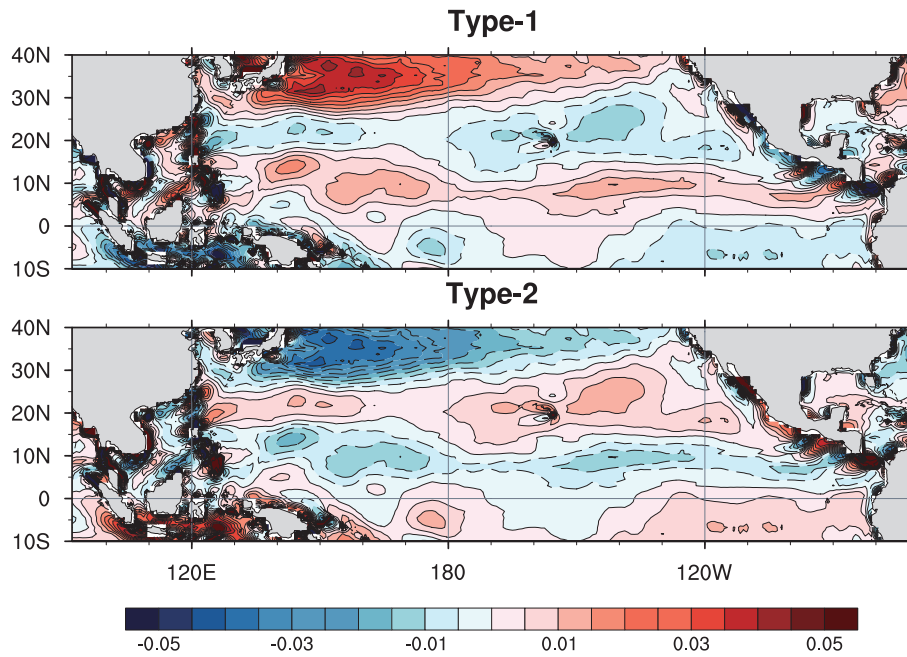


Fig. 8. Type-1 and -2 zonal wind stress errors (units: N m^{-2}).

7. Mechanisms responsible for the evolution of type-1 and -2 zonal wind stress errors

The evolutionary behavior of the simulation uncertainties caused by the two types of NFSV-like zonal wind stress errors is traced by calculating the annual mean simulation errors and time-dependent simulation errors along 18°N for each control run. Since similar results are obtained for the 25 control runs, we only take the control run of the year 1993 as an example to describe the results for simplicity. Figure 9 shows the corresponding SSH and depth-integrated current velocity components of the simulation errors induced by type-1 and -2 errors. It is shown that the SSH errors, influenced by a type-1 (type-2) error, present a large-scale pattern with negative (positive) anomalies in $10^\circ\text{--}20^\circ\text{N}$. The negative (positive) SSH error in $10^\circ\text{--}20^\circ\text{N}$ certainly corresponds to a current velocity error with the cyclonic (anticyclonic) circulation pattern. BK is located at the western boundary of the cyclonic (anticyclonic) circulation; thus, the current velocity errors at BK present negative (positive) anomalies with the effect of type-1 (type-2) errors. It is also worth noting that, in addition to the large-scale cyclonic (anticyclonic) SSH and depth-integrated current velocity errors, mesoscale eddy-like SSH errors exist around the latitude of BK (i.e., 18°N); specifically, in the region west of 150°E . To illustrate the evolution of the dominant errors in the region, we analyze the power spectrum of the simulation errors in the relative vorticity of sea surface velocity caused by type-1 and -2 errors and find that the power spectrum shows the peak at a period of 40–60 days (not shown). Filtering the simulation errors in the relative vorticity of sea surface velocity within a period of 40–60 days, we plot the time-dependent bandpass filter simulation errors in Fig. 10. The eddy-like structures can be clearly seen in Fig. 10, which is consistent with what is shown in Fig. 9. These

eddy-like errors initially appear in February east of 150°E ; they then propagate westwards and are simultaneously amplified before they finally accumulate at the western boundary and perturb the current velocity at BK (Fig. 10).

The above discussion suggests that the current velocity errors at BK caused by type-1 and -2 errors mainly result from the combined effects of large-scale velocity errors and mesoscale eddy-like velocity errors. Therefore, to address the influences of type-1 and -2 errors on the current velocity at BK, it is necessary to explore how type-1 and -2 errors induce the above large-scale velocity errors with circulation structures and what is the mechanism responsible for the mesoscale velocity errors with eddy-like structures.

It is well known that the interior of the North Pacific Subtropical Gyre, whose western boundary current is the Kuroshio, satisfies the Sverdrup relation, as described in Eq. (16) (Hautala et al., 1994; Jiang et al., 2006):

$$\beta V = \frac{1}{\rho_0} \text{curl} \boldsymbol{\tau}, \quad (16)$$

where V is the vertically integrated meridional volume transport; $\rho_0 = 1025.0 \text{ kg m}^{-3}$ is the reference density; $\boldsymbol{\tau}$ is the wind stress; and β is the meridional gradient of the Coriolis parameter. The Sverdrup relation suggests that the curl, rather than the magnitude, of the wind stress controls the meridional transport and therefore drives the general circulation in the subtropical North Pacific. The Sverdrup relation is no longer applicable at the western boundary because of dissipation, but the transport of the western boundary current can be regarded as compensating for the total interior meridional transport calculated from the Sverdrup relation (Stommel, 1948). Specifically, the transport of the western boundary current flows poleward (equatorward), while the total transport in the ocean interior flows equatorward (poleward).

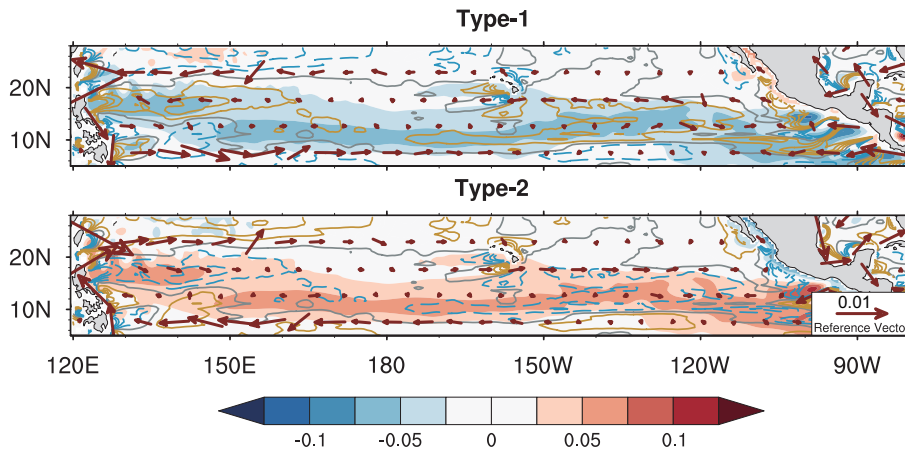


Fig. 9. Annual mean SSH (shaded; units: m) and depth-integrated velocity (vectors; units: m s^{-1}) components of simulation errors induced by type-1 and -2 errors for the control run of 1993 and the curl of zonal wind stress error (contours; units: 10^{-8} N m^{-3}) of type-1 and -2 errors. The blue dashed contours represent negative values, the yellow solid lines represent positive values, and the gray lines represent zero lines. The contour interval is $2 \times 10^{-8} \text{ N m}^{-3}$.

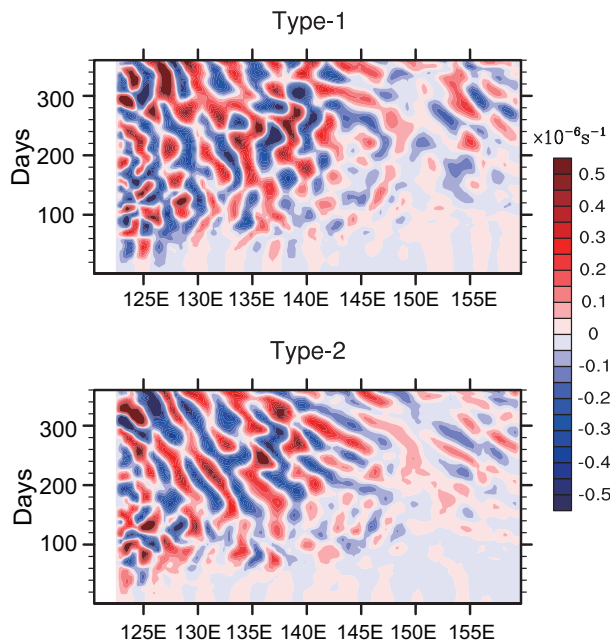


Fig. 10. The bandpass filter simulation errors in the relative vorticity of sea surface velocity caused by type-1 and -2 errors, which is calculated along 18°N for the control run of 1993 and filtered within the period of 40–60 days.

The fact that the motion of the subtropical North Pacific interior satisfies the Sverdrup relation encourages us to hypothesize that the meridional transport errors induced by the type-1 and -2 errors satisfy a mechanism similar to the Sverdrup relation. We confirm this mechanism by comparing the meridional volume transport errors (along the 18°N section) calculated by the meridional velocity error induced by the two types of NFSV-like errors and the Sverdrup relation. To facilitate this description, we hereafter refer to meridional volume transport as meridional transport. Specifically, we adopt Eq.

(17) to obtain the meridional transport errors induced by the NFSV-like errors and use Eq. (18) to obtain those from the Sverdrup relation:

$$G'_{\text{real}}(\lambda) = \int_{-D}^0 \int_{\lambda_e}^{\lambda} v' r_e \cos \phi d\lambda dz, \quad (17)$$

$$G'_{\text{sv}}(\lambda) = \frac{1}{\beta \rho_0} \int_{\lambda_e}^{\lambda} \text{curl} \boldsymbol{\tau}' r_e \cos \phi d\lambda, \quad (18)$$

where v' is the meridional velocity error; $\boldsymbol{\tau}'$ is the wind stress error; λ_e is the longitude of the eastern boundary; λ is the longitude of the western end point of the integration, which has values ranging from 250°E to 130°E ; $r_e = 6.371 \times 10^6 \text{ m}$ is the radius of the Earth; $\phi = 18^\circ\text{N}$ is the latitude; and D is the depth of the wind-driven layer. Hautala et al. (1994) demonstrated that depth-integrated geostrophic transport is not sensitive to the choice of D by comparing $D = 1000 \text{ m}$ with $D = 3000 \text{ m}$. Here, we choose the mean of these two values of D , i.e., $D = 2000 \text{ m}$, for the calculation in the present study.

The meridional transport error $G'_{\text{real}}(\lambda)$ induced by the type-1 and -2 errors is calculated using Eq. (17) for each perturbed simulation, and the annual mean is taken, while the corresponding Sverdrup transport error $G'_{\text{sv}}(\lambda)$ is calculated using Eq. (18). Figure 11 shows that the meridional transport errors $G'_{\text{real}}(\lambda)$ are positive for type-1 errors, negative for type-2 errors and in good agreement with the Sverdrup-related meridional transport errors $G'_{\text{sv}}(\lambda)$ at most longitudes along the 18°N section. Therefore, the meridional transport error $G'_{\text{real}}(\lambda)$ in the oceanic interior induced by type-1 and -2 errors can be approximated by the Sverdrup transport error $G'_{\text{sv}}(\lambda)$. This indicates that the curl, rather than the magnitude, of the wind stress errors controls the meridional transport errors in the 18°N section. That is, the positive (negative) meridional transport error in the oceanic interior induced by a type-1 (type-2) error is caused by the positive (negative) curl of the type-1 (type-2) error at the 18°N section. The BK is

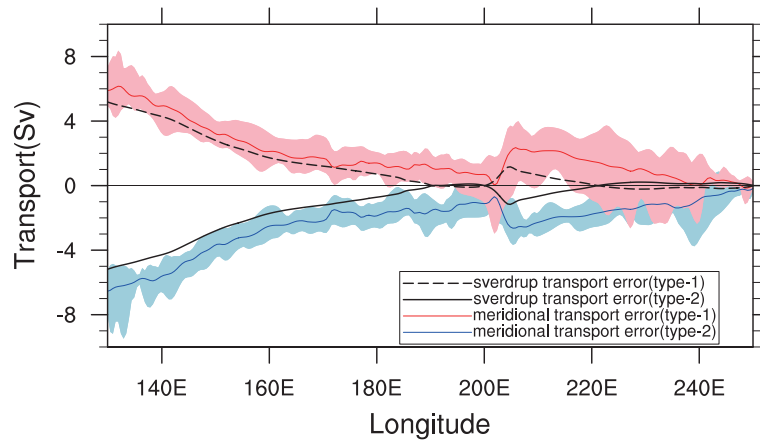


Fig. 11. The anomalous Sverdrup transport of type-1 (black dashed line) and -2 errors (black solid line) along 18°N and the mean (solid lines) and range (shaded) of the meridional transport (along 18°N) components of the simulation errors caused by type-1 (red) and -2 errors (blue) for the 25 control runs.

located at the western boundary of the Pacific. Hence, the type-1 (type-2) error-related meridional transport error at BK can be regarded as a compensation of the meridional transport error in the oceanic interior. Connected with the positive (negative) meridional transport error in the oceanic interior induced by a type-1 (type-2) error, that error induced by the type-1 (type-2) error at BK is therefore negative (positive). This point is also illustrated in Fig. 9. It is shown that the positive (negative) wind stress curl in 10° – 20°N across the Pacific basin of the type-1 (type-2) error leads to a negative (positive) SSH anomaly, which results in a (an) cyclonic (anticyclonic) circulation and thus a positive (negative) transport anomaly in the ocean interior, whereas a negative (positive) transport anomaly occurs at the western boundary and consequently leads to negative (positive) current velocity errors at BK.

We also show that the mesoscale eddy-like velocity errors in the region west of 150°E (near the BK) propagate westward and are simultaneously amplified. Generally, the existence and amplification of velocity errors with eddy-like structures are features of the instability of the concerned flows. These eddy-like errors appear at approximately 18°N , west of 150°E , which is in the region of the Subtropical Countercurrent. According to previous studies (Lien et al., 2014; Zhang et al., 2017), the westward propagating eddies in the Subtropical Countercurrent are generated due to the baroclinic instability of this region. In fact, we have shown that the Subtropical Countercurrent simulated by ROMS presents baroclinic instability similar to that in observations (see section 4.2); furthermore, the instability prefers to amplify the perturbation with a wavelength ranging from 299 km to 419 km, with the most unstable wavelength being approximately 355 km. Generally, the error with the most unstable wavelength grows fastest and will dominate the evolution. By estimating the wavelength of the eddy-like error caused by the type-1 and -2 zonal wind stress errors, there are approximately three eddies presenting in 10 degrees of longitude (see Fig. 10), which means that the wavelength of the eddy-like

errors is approximately 360 km and approximates the most unstable wavelength (355 km) of the baroclinic instability. That is, the dominant wavelength of the eddy-like errors induced by type-1 and -2 errors is close to the most unstable wavelength induced by the baroclinic instability. Therefore, we believe that baroclinic instability is the mechanism responsible for the amplification of eddy-like errors.

8. Implications of targeted observation for the simulation of the current velocity at BK

In section 5, it is demonstrated that the zonal wind stress error has the greatest impact on the simulation uncertainties in the current velocity at BK among all eight components of concern here. We obtain two types of NFSV-like errors, which significantly disturb the simulation of the current velocity at BK (see section 6). Furthermore, we explore the mechanism responsible for the evolution of simulation errors caused by NFSV-like errors (see section 7). We show that the curl of the NFSV-like zonal wind stress errors in 10° – 20°N has great influence on the simulation uncertainties in current velocity at the same latitudinal band and thus induces the simulation uncertainties at BK. Especially in the 18°N section, the current velocity error west of 150°E induced by the NFSV-like errors propagates westward and grows with the eddy-like structure because of the baroclinic instability. It seems that the errors outside of 10° – 20°N have nothing to do with the simulation uncertainties in the current velocity at BK.

The most disturbing errors can provide useful information on the sensitive areas for targeted observations. Although the NFSV-like errors here cannot equal the exact NFSV in Eq. (5) mathematically, and are not the most disturbing errors, they, compared with the error samples in **E**, have a more significant effect on the simulation of current velocity at BK. That is, the simulation uncertainties of current velocity at BK are significantly sensitive to the NFSV-like errors. Then, the sensitive

areas determined by these errors are certainly important for the targeted observations associated with the improvement in the simulation accuracy of the current velocity at BK. Previous studies have suggested that the regions where the most disturbing errors have a large value can be identified as potential sensitive areas for targeted observations, and reducing the errors in the sensitive areas results in great improvement in the simulation (or prediction) of the related events (Yu et al., 2012; Duan and Hu, 2016; Zhang et al., 2017; also see the introduction). Thus, the potential sensitive areas for targeted observation of the current velocity at BK can be determined in the 10°–20°N latitudinal band by identifying the regions where the curl of the NFSV-like wind stress errors is large. However, it is worth noting that the curl of the wind stress error near the eastern boundary in the latitudinal band is large but far away from BK (see Fig. 9). Considering that the phase speed of the western-propagating Rossby waves along 18°N is only approximately 0.09 m s^{-1} (Chelton and Schlax, 1996), it is conceivable that the wind stress error near the eastern boundary can hardly reach the western boundary during the one-year simulation and thus contributes little to the simulation uncertainties at BK. For identifying the sensitive areas for targeted observation of the current velocity at BK, the eastern boundary of the 10°–20°N latitudinal band can be ignored. We denote the region in the 10°–20°N latitudinal band extending from the western boundary to 110°W as the “Band-A” region. Then, the potential sensitive area can be

identified in this region.

To determine the potential sensitive areas, we prescribe an error curl value η . If the curl of the wind stress errors on spatial grids is larger than η , the corresponding grids can be regarded as those where the additional observations should be deployed, i.e., the sensitive areas for targeted observations. Therefore, the values of η determine the size of the sensitive area. We select values of η and make the number of grid points in the sensitive areas represent 2%, 4%, ..., 20% of the total number of grid points in Band-A. Then, we obtain 10 potential sensitive areas that are denoted as BA_2, BA_4, BA_6, ..., BA_20 (see Fig. 12). The improvements in the simulation accuracy of the current velocity at BK are estimated when the wind stress errors are removed in the potential sensitive areas. Specifically, we remove the wind stress error within the 10 sensitive areas from the type-1 and -2 errors and obtain 20 updated zonal wind stress errors. These updated zonal wind stress errors are then superimposed on each of the 25 control runs, and a total of 500 improved simulations are obtained. The 500 improved simulations are compared with the simulations perturbed by the type-1 and -2 errors, and the improvement in the simulation accuracy of the 25 control runs can be calculated using the formula $\text{Improvement} = (\Gamma_o - \Gamma_{o,\text{rm},\psi}) / \Gamma_o \times 100\%$, where $o = 1, 2$ and denotes the types of NFSV-like errors; $\psi = 1, 2, \dots, 10$ and represents the 10 potential sensitive areas BA_2, BA_4, BA_6, ..., BA_20; Γ_o is the annual mean of the simulation er-

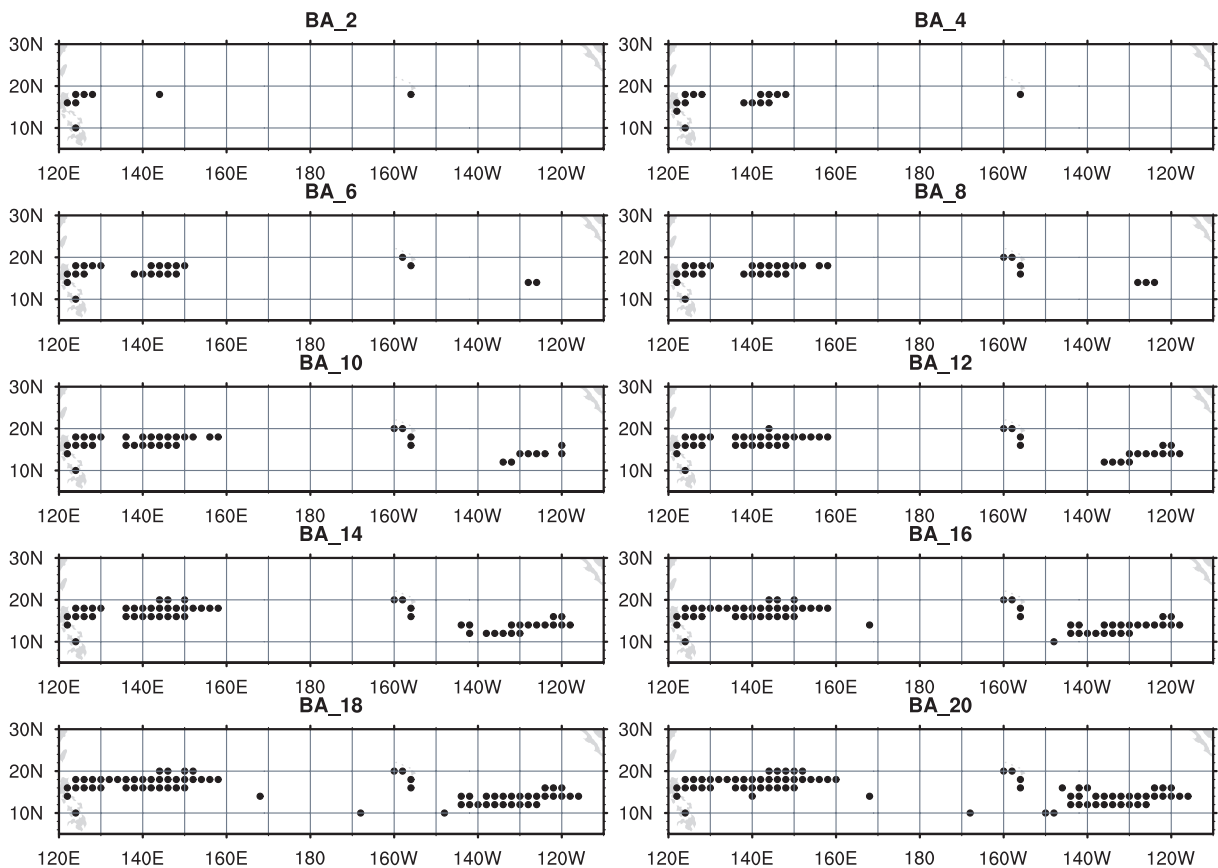


Fig. 12. Ten potential sensitive areas (dotted areas), which are denoted as BA_2, BA_4, ..., BA_20 in the text.

ror induced by a type- o error; and $\Gamma_{o,rm,\psi}$ is the annual mean of the simulation error induced by a type- o error but with the wind stress error in the ψ th sensitive area being removed. For each sensitive area, we can obtain 50 improved simulations (2×25 control runs) with the wind stress error in the sensitive areas being removed from the type-1 and -2 errors, and we use these simulations to characterize the improvement in the simulation accuracy of the current velocity at BK.

The box-and-whisker plot of these improvements is presented in Fig. 13. This figure shows that most simulation accuracies of the current velocity at BK can be improved by approximately 20% when removing the wind stress error in the sensitive area BA_2. When the size of the sensitive area increases to that of BA_4, the improvement in the simulation accuracy can reach approximately 40%. However, when the sizes of the sensitive areas continue to increase from BA_4 to BA_20, the improvements in the simulation accuracy remain at approximately 40%. This result indicates that deploying observations in the sensitive area BA_4 can increase the simulation accuracy of the current velocity at BK to the greatest extent, with the lowest cost. Therefore, the BA_4 region (see Fig. 12) represents the sensitive area for target observations associated with the simulation of the current velocity at BK. That is, one should preferentially deploy observations of the wind stress in the BA_4 region and assimilate them into the model to improve the accuracy of the external wind stress forcing and thus the simulation accuracy of the current velocity at BK.

As shown in Fig. 12, the BA_4 region mainly covers two areas. Both areas are located within the same latitudinal band, from 15°N to 20°N , but at different longitudes. The western area is located between the western boundary and the meridian of 130°E (which is near the BK). Obviously, the wind stress errors in that area locally influence the current velocity at BK. The eastern area is located from 140°E to 150°E . According to the results in section 7, the mesoscale eddy-like velocity errors breed there and are propagated to BK, finally perturbing the current velocity at BK. Obviously, the eastern area of the BA_4 region emphasizes the importance of the eddy-like errors in the simulation uncertainties in the current velocity at BK. Therefore, the reduction of the wind stress errors in the BA_4 region can significantly decrease both the wind stress errors influencing the BK locally and those influencing the BK by western-propagating eddy-like errors. Therefore, these two areas in the BA_4 region represent the sensitive areas for the targeted observations of external wind forcing associated with the simulation of the current velocity at BK. The determination of the sensitive area BA_4 also suggests that the additional observations near the eastern boundary contribute little to improving the simulation accuracy of the current velocity at BK and indicates that the wind stress errors located at the eastern boundary have little influence on the simulation errors in the current velocity at BK, which emphasizes that the exclusion of the eastern boundary with large wind stress errors from Band-A is feasible when determining the sensitive areas.

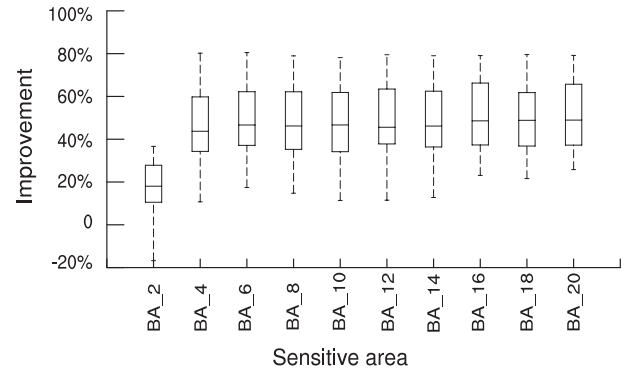


Fig. 13. Box-and-whisker plot of the improvement in the simulation accuracy of the current velocity at BK with respect to the 50 improved simulations (2×25 control runs) after removing the wind stress error in the sensitive areas of BA_2, BA_4, ..., BA_20 from type-1 and type-2 errors, where the simulation accuracy is measured by the extent of the reduction of the simulation errors.

9. Summary and discussion

In this study, we use ROMS to investigate the simulation uncertainties in the current velocity at BK induced by reanalysis errors under the perfect model assumption. Estimating the simulation uncertainties induced by the initial, boundary and forcing errors derived from different reanalysis datasets reveals that wind stress errors, especially zonal wind stress errors, induce the largest simulation uncertainties in the current velocity at BK, which indicates that the observations of zonal wind stress should be preferentially obtained to improve the simulation accuracy of the current velocity at BK.

Considering the large expenses associated with obtaining field observations throughout the entire ocean, the present study extends targeted observation to improve the initialization of numerical models to determine the observations needed to reduce the errors in external wind stress forcing in the simulations of the current velocity at BK.

Using an ensemble-based method, the zonal wind stress errors that significantly disturb the current velocity at BK are revealed based on a group of error samples derived from reanalysis datasets by the NFSV approach, and two types of NFSV-like zonal wind stress errors are found to cause the largest simulation uncertainties in the current velocity at BK. The type-1 error exhibits a pattern of positive anomalies covering the two zonal bands of 0° – 15°N and 25° – 40°N in the Pacific Ocean, with negative anomalies appearing between these two bands. The type-2 error exhibits a pattern similar to that of the type-1 error but with opposite sign. These two types of errors possess one dominant EOF mode but cause negative and positive errors, respectively, in the current velocity at BK in one-year simulations. Exploring the evolution of the simulation errors caused by the NFSV-like errors reveals that these simulation errors result from the combined effects of large-scale circulation errors and mesoscale eddy-like velocity errors induced by type-1 and -2 errors. The large-scale circulation errors emphasize the role of the curl

of the wind stress error induced by the type-1 and -2 errors in yielding simulation uncertainties. Specifically, the type-1 (type-2) zonal wind stress errors induce positive (negative) curls of wind stress within the band of 10° – 20° N across the Pacific basin, which then excite a large-scale negative (positive) SSH anomaly and an anomalous cyclonic (anticyclonic) circulation there. The anomalous cyclonic (anticyclonic) circulation results in positive (negative) transport in the ocean interior but negative (positive) transport at the western boundary. Then, the current velocity at BK located at the western boundary is perturbed by a negative (positive) velocity anomaly, indicating a negative (positive) error occurring in the current velocity at BK. The mesoscale eddy-like velocity errors induced by the type-1 and -2 errors are located near the latitude of BK (i.e., 18° N) and perturb the current velocity there. The eddy-like errors appear in the region west of 150° E, propagate westward with amplified intensities and finally accumulate at the western boundary to perturb the current velocity at BK. The baroclinic instability induced by the Subtropical Countercurrent and Northern Equatorial Current is responsible for the existence and amplification of eddy-like errors, which is analogous to the mechanism of the generation of mesoscale eddies.

The above results indicate that the curl of the wind stress error influences the current velocity at BK. Particularly, the large curl values of the type-1 and -2 errors that are located within Band-A (i.e., the region along 10° – 20° N and from the western boundary to 110° W) contribute most to the simulation errors in the current velocity at BK. This indicates that the sensitive area for targeted observations associated with the simulation of the current velocity at BK may be located in Band-A. Experiments revealed that two sensitive areas exist in Band-A: one covers the region along 15° N– 20° N but extends from BK to the west of 130° E, and the other is located in the region along 15° – 20° N but extends from 140° – 150° E. The wind stress errors in the former area locally influence the current velocity at BK, while those in the latter area tend to induce eddy-like errors that are subsequently propagated to BK and influence the current velocity there. Therefore, the additional observations in these two areas can not only reduce the wind stress errors locally influencing BK but also decrease those of the western-propagating eddy-like errors, thus efficiently improving the simulation accuracy for the BK velocity. These two areas may represent the sensitive areas for targeted observations associated with the simulation of the current velocity at BK.

The above results show that one of the sensitive areas breeds the eddy-like errors induced by the external wind stress forcing and emphasize the importance of the eddy-like errors in yielding the simulation uncertainties in the current velocity at BK. This suggests that reducing the eddy-like errors in this area may greatly decrease the simulation errors in the current velocity at BK, which also sheds light on the non-negligible role of mesoscale processes in the Kuroshio Current. Of course, this also reflects the importance of using fine-grid observations to reduce eddy-like errors and thus to improve the simulation accuracy of the current velocity at

BK. However, obtaining fine-grid observations is challenging. It is thus expected that an efficient observational strategy can be designed to address this challenge.

In the present study, we consider the simulation uncertainties caused by reanalysis data errors. We consult the NFSV approach and identify the disturbing constant zonal wind stress errors to the current velocity at BK by an ensemble-based method (Duan et al., 2009; Duan and Wei, 2013; Duan and Zhou, 2013; Duan and Hu, 2016). Here, this method is assumed to make the ensemble samples sufficiently diversified to represent all possible zonal wind stress errors, such that the characteristics of the theoretical NFSV can be captured by the NFSV-like errors. However, this assumption is not necessarily true. Hence, a more effective algorithm should be developed to compute the theoretical NFSV, and the results shown in the present study can be further investigated. Moreover, the NFSV-like errors and the sensitive areas identified in the present study are dependent on ROMS with a certain configuration. Whether the results we obtained depend on the simulation system needs to be explored in future studies. Finally, the disturbing wind stress errors here are assumed to be time-independent of the current velocity at BK. This assumption is too strong, and it is necessary to investigate the effect of time-dependent wind stress errors on the current velocity at BK.

Acknowledgements. This work was jointly sponsored by the Strategic Priority Research Program of the Chinese Academy of Sciences (Grant No. XDA11010303) and the National Natural Science Foundation of China (Grant No. 41525017). ROMS is open source and can be downloaded from <https://www.myroms.org/>. The present study adopted data from GODAS, CORE.v2, SODA 2.1.6, and ERA-Interim. They can be obtained from <https://www.esrl.noaa.gov/psd/data/gridded/data.godas.html>, <http://data1.gfdl.noaa.gov/nomads/forms/core/COREv2.html>, http://apdrc.soest.hawaii.edu/datadoc/soda_2.1.6.php, <http://apps.ecmwf.int/datasets/data/interim-full-daily/levtype=sfc/> and http://icdc.cen.uni-hamburg.de/1/projekte/easy-init/easy-init-ocean.html?no_cache=1, respectively.

REFERENCES

- Balmaseda, M. A., A. Vidard, and D. L. T. Anderson, 2008: The ECMWF ocean analysis system: ORA-S3. *Mon. Wea. Rev.*, **136**, 3018–3034, <https://doi.org/10.1175/2008MWR2433.1>.
- Behringer, D. W., Y. Xue, 2004: Evaluation of the global ocean data assimilation system at NCEP: The Pacific Ocean. *Eighth Symposium on Integrated Observing and Assimilation Systems for Atmosphere, Oceans, and Land Surface, AMS 84th Annual Meeting*, Washington State Convention and Trade Center, Seattle, Washington, 11–15.
- Carton, J. A., and B. S. Giese, 2008: A reanalysis of ocean climate using simple ocean data assimilation (SODA). *Mon. Wea. Rev.*, **136**, 2999–3017, <https://doi.org/10.1175/2007MWR1978.1>.
- Centurioni, L. R., P. P. Niiler, and D.-K. Lee, 2004: Observations of inflow of philippine sea surface water into the South China Sea through the Luzon Strait. *J. Phys. Oceanogr.*, **34**, 113–121, [https://doi.org/10.1175/1520-0485\(2004\)034](https://doi.org/10.1175/1520-0485(2004)034)

<0113:OOIOPS>2.0.CO;2.

- Chelton, D. B., and M. G. Schlax, 1996: Global observations of oceanic rossby waves. *Science*, **272**, 234–238, <https://doi.org/10.1126/science.272.5259.234>.
- Dee, D. P., and Coauthors, 2011: The ERA-Interim reanalysis: Configuration and performance of the data assimilation system. *Quart. J. Roy. Meteor. Soc.*, **137**, 553–597, <https://doi.org/10.1002/qj.828>.
- Du, C., and Coauthors, 2013: Impact of the Kuroshio intrusion on the nutrient inventory in the upper northern South China Sea: Insights from an isopycnal mixing model. *Biogeosciences*, **10**, 6419–6432, <https://doi.org/10.5194/bg-10-6419-2013>.
- Duan, W. S., and C. Wei, 2013: The ‘spring predictability barrier’ for ENSO predictions and its possible mechanism: Results from a fully coupled model. *International Journal of Climatology*, **33**, 1280–1292, <https://doi.org/10.1002/joc.3513>.
- Duan, W. S., and P. Zhao, 2015: Revealing the most disturbing tendency error of Zebiak–Cane model associated with El Niño predictions by nonlinear forcing singular vector approach. *Climate Dyn.*, **44**, 2351–2367, <https://doi.org/10.1007/s00382-014-2369-0>.
- Duan, W. S., and F. F. Zhou, 2013: Non-linear forcing singular vector of a two-dimensional quasi-geostrophic model. *Tellus A*, **65**, 18452, <https://doi.org/10.3402/tellusa.v65i0.18452>.
- Duan, W. S., and J. Y. Hu, 2016: The initial errors that induce a significant “spring predictability barrier” for El Niño events and their implications for target observation: Results from an earth system model. *Climate Dyn.*, **46**, 3599–3615, <https://doi.org/10.1007/s00382-015-2789-5>.
- Duan, W. S., X. C. Liu, K. Y. Zhu, and M. Mu, 2009: Exploring the initial errors that cause a significant “spring predictability barrier” for El Niño events. *J. Geophys. Res.*, **114**, C04022, <https://doi.org/10.1029/2008JC004925>.
- Fang, G. H., W. Fang, Y. Fang, and K. Wang, 1998: A survey of studies on the South China Sea upper ocean circulation. *Acta Oceanogr. Taiwanica*, **37**, 1–16.
- Fujii, Y., H. Tsujino, N. Usui, H. Nakano, and M. Kamachi, 2008: Application of singular vector analysis to the Kuroshio large meander. *J. Geophys. Res.*, **113**, C07026, <https://doi.org/10.1029/2007JC004476>.
- Gordon, A. L., P. Flament, C. Villanoy, and L. Centurioni, 2014: The nascent Kuroshio of Lamon Bay. *J. Geophys. Res.*, **119**, 4251–4263, <https://doi.org/10.1002/2014JC009882>.
- Gu, D.-F., and S. G. H. Philander, 1997: Interdecadal climate fluctuations that depend on exchanges between the tropics and extratropics. *Science*, **275**, 805–807, <https://doi.org/10.1126/science.275.5301.805>.
- Haidvogel, D. B., H. G. Arango, K. Hedstrom, A. Beckmann, P. Malanotte-Rizzoli, and A. F. Shchepetkin, 2000: Model evaluation experiments in the North Atlantic Basin: Simulations in nonlinear terrain-following coordinates. *Dyn. Atmos. Oceans*, **32**, 239–281, [https://doi.org/10.1016/S0377-0265\(00\)00049-X](https://doi.org/10.1016/S0377-0265(00)00049-X).
- Haidvogel, D. B., and Coauthors, 2008: Ocean forecasting in terrain-following coordinates: Formulation and skill assessment of the Regional Ocean Modeling System. *J. Comput. Phys.*, **227**, 3595–3624, <https://doi.org/10.1016/j.jcp.2007.06.016>.
- Hautala, S. L., D. H. Roemmich, and W. J. Schmitz, Jr., 1994: Is the North Pacific in Sverdrup balance along 24°N? *J. Geophys. Res.*, **99**, 16 041–16 052, <https://doi.org/10.1029/94JC01084>.
- Hu, D. X., and M. C. Cui, 1991: The Western Boundary Current of the Pacific and its role in the climate. *Chinese Journal of Oceanology and Limnology*, **9**, 1–14, <https://doi.org/10.1007/BF02849784>.
- Hu, D. X., and Coauthors, 2013: Direct measurements of the Luzon undercurrent. *J. Phys. Oceanogr.*, **43**, 1417–1425, <https://doi.org/10.1175/JPO-D-12-0165.1>.
- Hu, D. X., and Coauthors, 2015: Pacific western boundary currents and their roles in climate. *Nature*, **522**, 299–308, <https://doi.org/10.1038/nature14504>.
- Jan, S., and Coauthors, 2015: Large variability of the Kuroshio at 23.75°N east of Taiwan. *J. Geophys. Res.*, **120**, 1825–1840, <https://doi.org/10.1002/2014JC010614>.
- Jiang, H., H. Wang, J. Zhu, and B. K. Tan, 2006: Relationship between real meridional volume transport and Sverdrup transport in the North Subtropical Pacific. *Chinese Science Bulletin*, **51**, 1757–1760, <https://doi.org/10.1007/s11434-006-2031-2>.
- Kanamitsu, M., W. Ebisuzaki, J. Woollen, S. K. Yang, J. J. Hnilo, M. Fiorino, and G. L. Potter, 2002: NCEP-DOE AMIP-II reanalysis (R-2). *Bull. Amer. Meteor. Soc.*, **83**, 1631–1644, <https://doi.org/10.1175/BAMS-83-11-1631>.
- Kaneko, A., M., and Coauthors, 1998: ADCP observation of the western equatorial Pacific by a commercial ship. *Umi*, **7**(6), 357–368, <https://doi.org/10.5928/kaiyou.7.357>.
- Kashino, Y., N. España, F. Syamsudin, K. J. Richards, T. Jensen, P. Dutrieux, and A. Ishida, 2009: Observations of the north equatorial current, Mindanao current, and Kuroshio current system during the 2006/07 El Niño and 2007/08 La Niña. *Journal of Oceanography*, **65**, 325–333, <https://doi.org/10.1029/2000GL011630>.
- Kim, Y. Y., T. D. Qu, T. Jensen, T. Miyama, H. Mitsudera, H. W. Kang, and A. Ishida, 2004: Seasonal and interannual variations of the north equatorial current bifurcation in a high-resolution OGCM. *J. Geophys. Res.*, **109**, C03040, <https://doi.org/10.1029/2003JC002013>.
- Large, W. G., and S. G. Yeager, 2009: The global climatology of an interannually varying air–sea flux data set. *Climate Dyn.*, **33**, 341–364, <https://doi.org/10.1007/s00382-008-0441-3>.
- Latif, M., and T. P. Barnett, 1994: Causes of decadal climate variability over the North Pacific and North America. *Science*, **266**, 634–637, <https://doi.org/10.1126/science.266.5185.634>.
- Li, J. J., X. Jiang, G. Li, Z. Y. Jing, L. B. Zhou, Z. X. Ke, and Y. H. Tan, 2017: Distribution of picoplankton in the northeastern South China Sea with special reference to the effects of the Kuroshio intrusion and the associated mesoscale eddies. *Science of the Total Environment*, **589**, 1–10, <https://doi.org/10.1016/j.scitotenv.2017.02.208>.
- Lien, R.-C., B. Ma, Y. H. Cheng, C. R. Ho, B. Qiu, C. M. Lee, and M. H. Chang, 2014: Modulation of Kuroshio transport by mesoscale eddies at the Luzon Strait entrance. *J. Geophys. Res.*, **119**, 2129–2142, <https://doi.org/10.1002/2013JC009548>.
- Lien, R.-C., and Coauthors, 2015: The Kuroshio and Luzon undercurrent east of Luzon Island. *Oceanography*, **28**, 54–63, <https://doi.org/10.5670/oceanog.2015.81>.
- Lu, J., and Q. Liu, 2013: Gap-leaping Kuroshio and blocking westward-propagating Rossby wave and eddy in the Luzon Strait. *J. Geophys. Res.*, **118**(3), 1170–1181, <https://doi.org/10.1002/jgrc.20116>.
- Macdonald, A. M., and C. Wunsch, 1996: An estimate of global ocean circulation and heat fluxes. *Nature*, **382**, 436–439,

- <https://doi.org/10.1038/382436a0>.
- Majumdar, S. J., 2016: A review of targeted observations. *Bull. Amer. Meteor. Soc.*, **97**, 2287–2303, <https://doi.org/10.1175/BAMS-D-14-00259.1>.
- McCreary, J. P. Jr., and P. Lu, 1994: Interaction between the subtropical and equatorial ocean circulations: The subtropical cell. *J. Phys. Oceanogr.*, **24**, 466–497, [https://doi.org/10.1175/1520-0485\(1994\)024<0466:IBTSAE>2.0.CO;2](https://doi.org/10.1175/1520-0485(1994)024<0466:IBTSAE>2.0.CO;2).
- Mu, M., 2013: Methods, current status, and prospect of targeted observation. *Science China Earth Sciences*, **56**, 1997–2005, <https://doi.org/10.1007/s11430-013-4727-x>.
- Nakano, T., I. Kaneko, M. Endoh, and M. Kamachi, 2005: Interannual and decadal variabilities of npiw salinity minimum core observed along jma's hydrographic repeat sections. *Journal of Oceanography*, **61**(4), 681–697, <https://doi.org/10.1007/s10872-005-0076-5>.
- Nan, F., H. J. Xue, F. Chai, L. Shi, M. C. Shi, and P. F. Guo, 2011: Identification of different types of Kuroshio intrusion into the South China Sea. *Ocean Dynamics*, **61**, 1291–1304, <https://doi.org/10.1007/s10236-011-0426-3>.
- Nan, F., F. Yu, H. J. Xue, L. L. Zeng, D. X. Wang, S. L. Yang, and K. C. Nguyen, 2016: Freshening of the upper ocean in the South China Sea since the early 1990s. *Deep Sea Research Part I: Oceanographic Research Papers*, **118**, 20–29, <https://doi.org/10.1016/j.dsr.2016.10.010>.
- Nitani, H., 1972: Beginning of the Kuroshio. *Kuroshio: Physical Aspects of the Japan Current*, H. Stommel and K. Yashida., Eds., University of Washington Press, 129–163.
- Prakash, K. R., and V. Pant, 2017: Upper oceanic response to tropical cyclone Phailin in the Bay of Bengal using a coupled atmosphere-ocean model. *Ocean Dynamics*, **67**, 51–64, <https://doi.org/10.1007/s10236-016-1020-5>.
- Qiu, B., 1999: Seasonal eddy field modulation of the North Pacific subtropical countercurrent: TOPEX/Poseidon observations and theory. *J. Phys. Oceanogr.*, **29**, 2471–2486, [https://doi.org/10.1175/1520-0485\(1999\)029<2471:SEFMOT>2.0.CO;2](https://doi.org/10.1175/1520-0485(1999)029<2471:SEFMOT>2.0.CO;2).
- Qiu, B., and R. Lukas, 1996: Seasonal and interannual variability of the North Equatorial Current, the Mindanao Current, and the Kuroshio along the Pacific western boundary. *J. Geophys. Res.*, **101**, 12 315–12 330, <https://doi.org/10.1029/95JC03204>.
- Qiu, B., and S. M. Chen, 2010: Interannual variability of the North Pacific subtropical countercurrent and its associated mesoscale eddy field. *J. Phys. Oceanogr.*, **40**, 213–225, <https://doi.org/10.1175/2009JPO4285.1>.
- Qiu, B., T. Nakano, S. M. Chen, and P. Klein, 2017: Submesoscale transition from geostrophic flows to internal waves in the northwestern Pacific upper ocean. *Nature Communications*, **8**, 14055, <https://doi.org/10.1038/ncomms14055>.
- Qu, T. D., H. Mitsudera, and T. Yamagata, 1998: On the western boundary currents in the Philippine Sea. *J. Geophys. Res.*, **103**, 7537–7548, <https://doi.org/10.1029/98JC00263>.
- Qu, T. D., Y. Y. Kim, M. Yaremchuk, T. Tozuka, A. Ishida, and T. Yamagata, 2004: Can Luzon Strait transport play a role in conveying the impact of ENSO to the South China Sea?. *J. Climate*, **17**, 3644–3657, [https://doi.org/10.1175/1520-0442\(2004\)017<3644:CLSTPA>2.0.CO;2](https://doi.org/10.1175/1520-0442(2004)017<3644:CLSTPA>2.0.CO;2).
- Rudnick, D. L., and Coauthors, 2011: Seasonal and mesoscale variability of the Kuroshio near its origin. *Oceanography*, **24**, 52–63, <https://doi.org/10.5670/oceanog.2011.94>.
- Shchepetkin, A. F., and J. C. McWilliams, 2003: A method for computing horizontal pressure-gradient force in an oceanic model with a nonaligned vertical coordinate. *J. Geophys. Res.*, **108**, 3090, <https://doi.org/10.1029/2001JC001047>.
- Shchepetkin, A. F., and J. C. McWilliams, 2005: The regional oceanic modeling system (ROMS): A split-explicit, free-surface, topography-following-coordinate oceanic model. *Ocean Modelling*, **9**, 347–404, <https://doi.org/10.1016/j.ocemod.2004.08.002>.
- Sheremet, V. A., and J. Kuehl, 2007: Gap-leaping western boundary current in a circular tank model. *J. Phys. Oceanogr.*, **37**, 1488–1495, <https://doi.org/10.1175/JPO3069.1>.
- Song, Y. H., and D. Haidvogel, 1994: A semi-implicit ocean circulation model using a generalized topography-following coordinate system. *J. Comput. Phys.*, **115**, 228–244, <https://doi.org/10.1006/jcph.1994.1189>.
- Stommel, H., 1948: The westward intensification of wind-driven ocean currents. *Eos, Trans. Amer. Geophys. Union*, **29**, 202–206, <https://doi.org/10.1029/TR029i002p00202>.
- Tao, L. J., R.-H. Zhang, and C. Gao, 2017: Initial error-induced optimal perturbations in ENSO predictions, as derived from an intermediate coupled model. *Adv. Atmos. Sci.*, **34**(6), 791–803, <https://doi.org/10.1007/s00376-017-6266-4>.
- Trenberth, K. E., and J. M. Caron, 2001: Estimates of meridional atmosphere and ocean heat transports. *J. Climate*, **14**, 3433–3443, [https://doi.org/10.1175/1520-0442\(2001\)014<3433:EOMAAO>2.0.CO;2](https://doi.org/10.1175/1520-0442(2001)014<3433:EOMAAO>2.0.CO;2).
- Wang, F., N. Zang, Y. L. Li, and D. X. Hu, 2015: On the subsurface countercurrents in the Philippine Sea. *J. Geophys. Res.*, **120**, 131–144, <https://doi.org/10.1002/2013JC009690>.
- Wang, Q., and M. Mu, 2015: A new application of conditional nonlinear optimal perturbation approach to boundary condition uncertainty. *J. Geophys. Res.*, **120**(12), 7979–7996, <https://doi.org/10.1002/2015JC011095>.
- Wang, Q., M. Mu, and H. A. Dijkstra, 2013: The similarity between optimal precursor and optimally growing initial error in prediction of Kuroshio large meander and its application to targeted observation. *J. Geophys. Res.*, **118**, 869–884, <https://doi.org/10.1002/jgrc.20084>.
- Wang, Q. Y., and D. X. Hu, 2012: Origin of the Luzon undercurrent. *Bulletin of Marine Science*, **88**, 51–60, <https://doi.org/10.5343/bms.2011.1020>.
- Wunsch, C., 2005: The total meridional heat flux and its oceanic and atmospheric partition. *J. Climate*, **18**, 4374–4380, <https://doi.org/10.1175/JCLI3539.1>.
- Xiao, F., L. L. Zeng, Q. Y. Liu, W. Zhou, and D. X. Wang, 2018: Extreme subsurface warm events in the South China Sea during 1998/99 and 2006/07: Observations and mechanisms. *Climate Dyn.*, **50**, 115–128, <https://doi.org/10.1007/s00382-017-3588-y>.
- Yu, Y., Mu, M., W. Duan, and T. Gong, 2012: Contribution of the location and spatial pattern of initial error to uncertainties in El Niño predictions. *J. Geophys. Res.*, **117**, <https://doi.org/10.1029/2011JC007758>.
- Zhai, F. G., D. X. Hu, Q. Y. Wang, and F. J. Wang, 2014: Long-term trend of Pacific South Equatorial Current bifurcation over 1950–2010. *Geophys. Res. Lett.*, **41**, 3172–3180, <https://doi.org/10.1002/2014GL059934>.
- Zhang, K., Q. Wang, M. Mu, and P. Liang, 2016: Effects of optimal initial errors on predicting the seasonal reduction of the upstream Kuroshio transport. *Deep Sea Research Part I: Oceanographic Research Papers*, **116**, 220–235, <https://doi.org/10.1016/j.dsr.2016.08.008>.

- Zhang, K., M. Mu, and Q. Wang, 2017: Identifying the sensitive area in adaptive observation for predicting the upstream Kuroshio transport variation in a 3-D ocean model. *Science China Earth Sciences*, **60**, 866–875, <https://doi.org/10.1007/s11430-016-9020-8>.
- Zhao, Y. P., and G. A. McBean, 1986: Annual and interannual variability of the North Pacific ocean-to-atmosphere total heat transfer. *Atmos.-Ocean*, **24**, 265–282, <https://doi.org/10.1080/07055900.1986.9649251>.
- Zou, G. A., Q. Wang, and M. Mu, 2016: Identifying sensitive areas of adaptive observations for prediction of the Kuroshio large meander using a shallow-water model. *Chinese Journal of Oceanology and Limnology*, **34**, 1122–1133, <https://doi.org/10.1007/s00343-016-4264-5>.